Dynamic soil-structure interaction: A three-dimensional numerical approach and its application to the Lotung case study

Elsevier Editorial System(tm) for Computers and Geotechnics

Manuscript Draft

Manuscript Number: COGE-D-16-00897R2

Title: Dynamic Soil-Structure Interaction: a three-dimensional numerical approach and its application to the Lotung case study

Article Type: Research Paper

Keywords: Dynamic soil-structure interaction; seismic ground response; FE numerical modelling; direct method; Lotung LSST; multidirectional loading conditions

Corresponding Author: Professor ANGELO AMOROSI, Ph.D.

Corresponding Author's Institution: Sapienza University of Rome

First Author: ANGELO AMOROSI, Ph.D.

Order of Authors: ANGELO AMOROSI, Ph.D.; Daniela Boldini, Ph.D.; Annamaria di Lernia, Ph.D.

Abstract: The paper presents a 3D non-linear finite element approach to analyse the dynamic SSI phenomena observed at the Lotung Large-Scale Seismic Test site. The study is performed in the time domain accounting for the non-linear behaviour of soil and the multi-directional nature of seismic events. The approach is first validated simulating simplified cases for which analytical solutions exist. Then, it is adopted to satisfactorily back-analyse the seismic behaviour of the 1/4-scale nuclear power plant containment structure constructed at the site. This research proves that dynamic SSI can be tackled by direct approach, overpassing the strong simplifications of better-established substructure schemes.

Figure 1

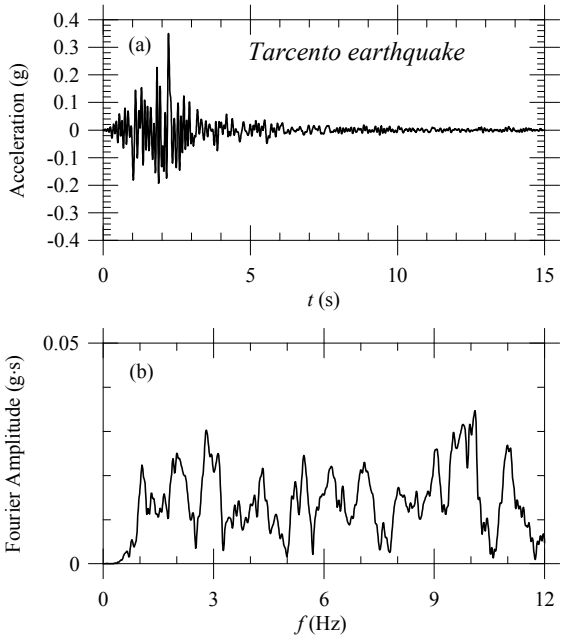
(a)
Tarcento earthquake
Acceleration (g)
0.4
0.3
0.2
0.1
0
-0.1
-0.2
-0.3
-0.4
0
5
10
15
t (s)
(b)
Fourier Amplitude (g·s)
0.05
0
0
3
6
9
12
f (Hz)

Figure 2

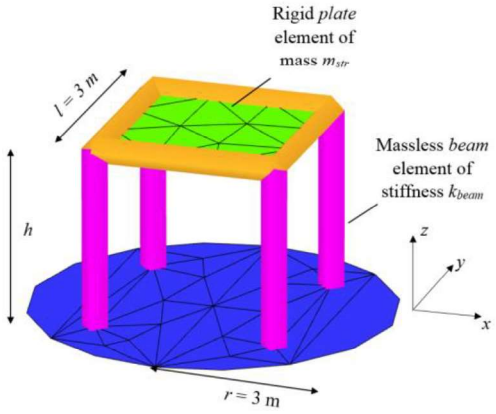
Rigid *plate*
element of
mass m_{str}
$l = 3\ m$
Massless *beam*
element of
stiffness k_{beam}
h
z
y
x
$r = 3$ m

Figure 3

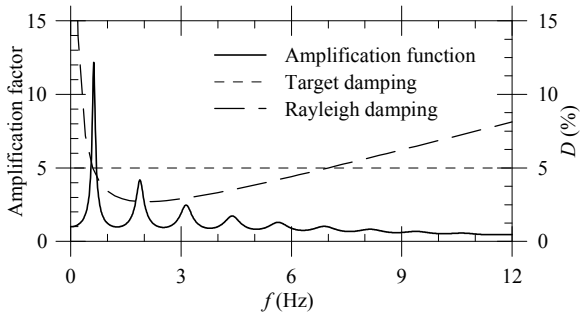
15
10
5
0
0
3
6
9
12
f (Hz)
Amplification factor
D (%)
Amplification function
Target damping
Rayleigh damping

Figure 4

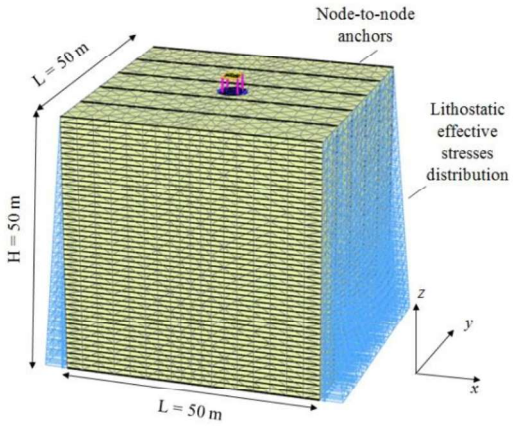
Node-to-node
anchors
L = 50 m
Lithostatic
effective
stresses
distribution
H = 50 m
z
y
x
L = 50 m

Figure 5

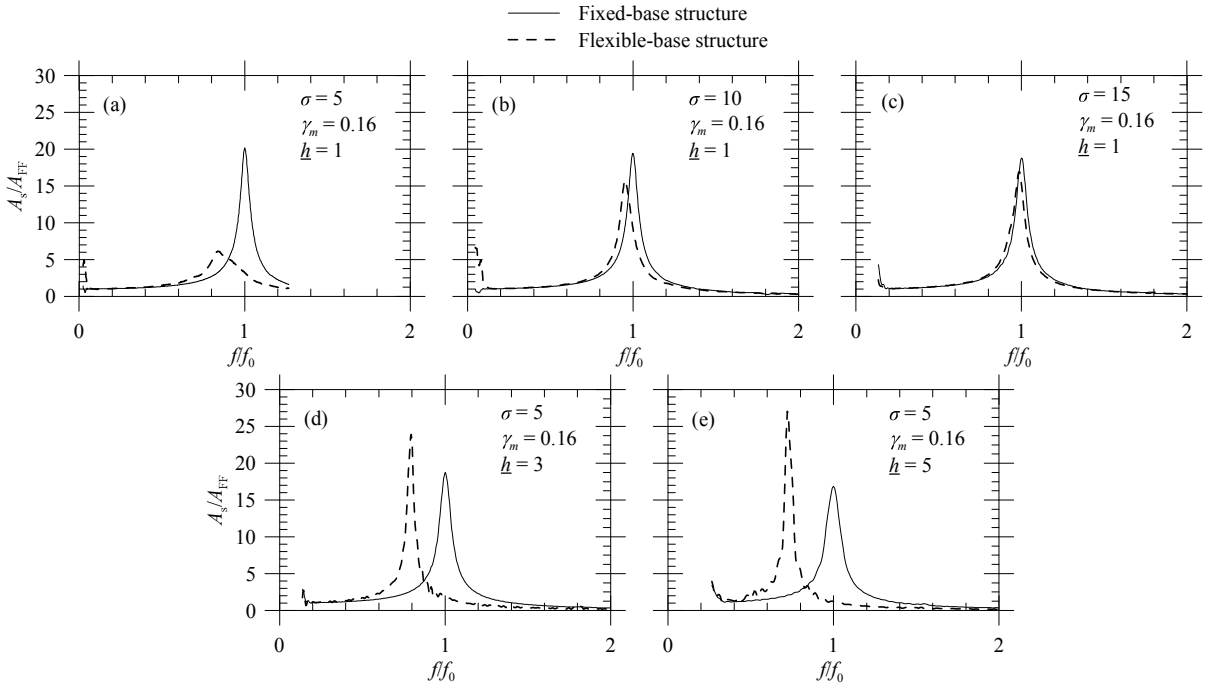
Fixed-base structure
Flexible-base structure
(a)
σ = 5
γm = 0.16
h = 1
(b)
σ = 10
γm = 0.16
h = 1
(c)
σ = 15
γm = 0.16
h = 1
(d)
σ = 5
γm = 0.16
h = 3
(e)
σ = 5
γm = 0.16
h = 5
As/AFF
f/f0

Figure 6

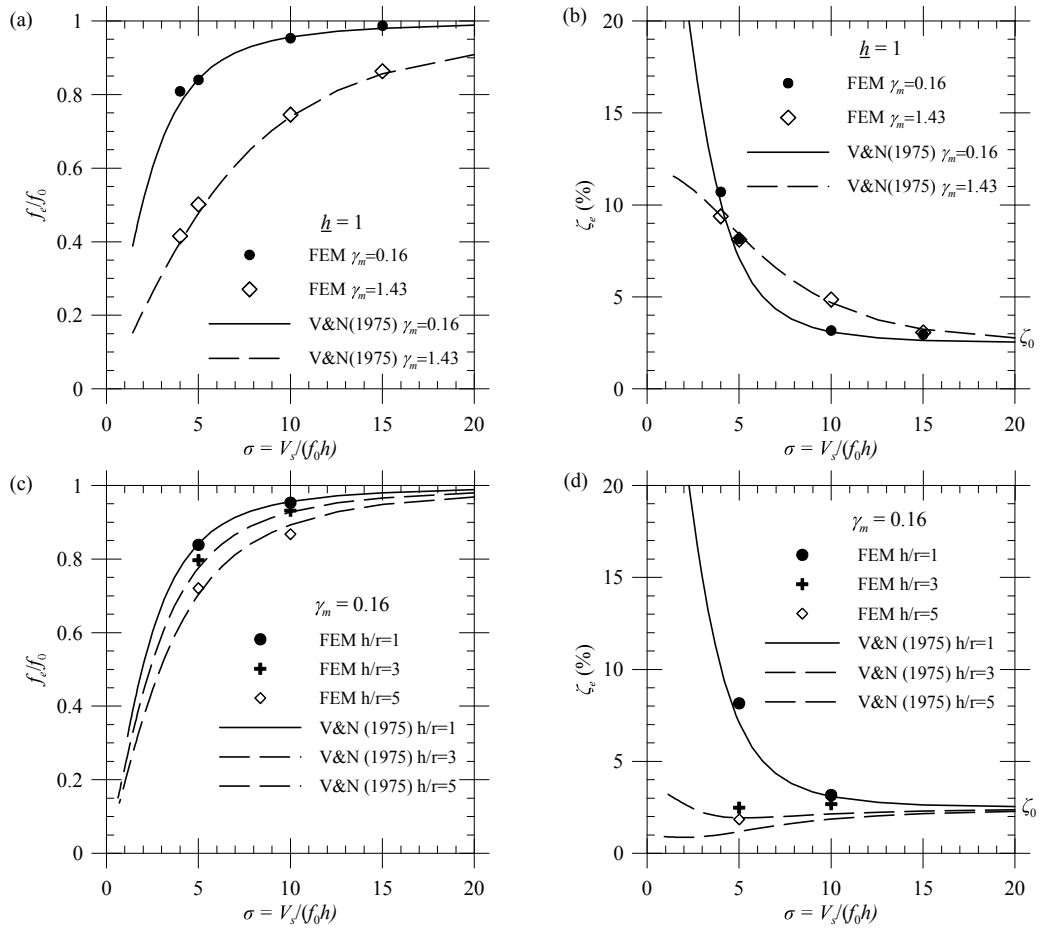
(a)
f_e/f_0
$\underline{h}$ = 1
FEM γ_m=0.16
FEM γ_m=1.43
V&N(1975) γ_m=0.16
V&N(1975) γ_m=1.43
$\sigma = V_s/(f_0 h)$
(b)
ζ_e (%)
$\underline{h}$ = 1
FEM γ_m=0.16
FEM γ_m=1.43
V&N(1975) γ_m=0.16
V&N(1975) γ_m=1.43
ζ_0
$\sigma = V_s/(f_0 h)$
(c)
f_e/f_0
γ_m = 0.16
FEM h/r=1
FEM h/r=3
FEM h/r=5
V&N (1975) h/r=1
V&N (1975) h/r=3
V&N (1975) h/r=5
$\sigma = V_s/(f_0 h)$
(d)
ζ_e (%)
γ_m = 0.16
FEM h/r=1
FEM h/r=3
FEM h/r=5
V&N (1975) h/r=1
V&N (1975) h/r=3
V&N (1975) h/r=5
ζ_0
$\sigma = V_s/(f_0 h)$

Figure 7

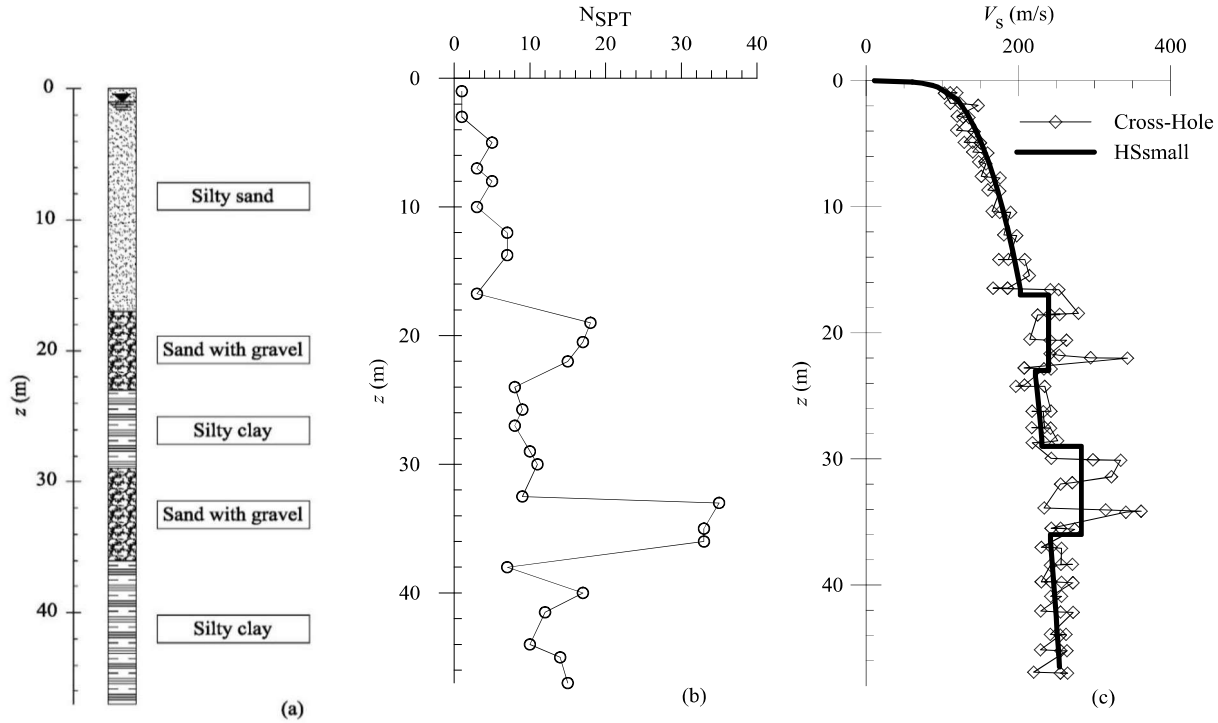
0
10
20
30
40
z (m)
Silty sand
Sand with gravel
Silty clay
Sand with gravel
Silty clay
(a)
N_SPT
0
10
20
30
40
z (m)
(b)
V_S (m/s)
0
200
400
Cross-Hole
HSsmall
z (m)
(c)

Figure 8

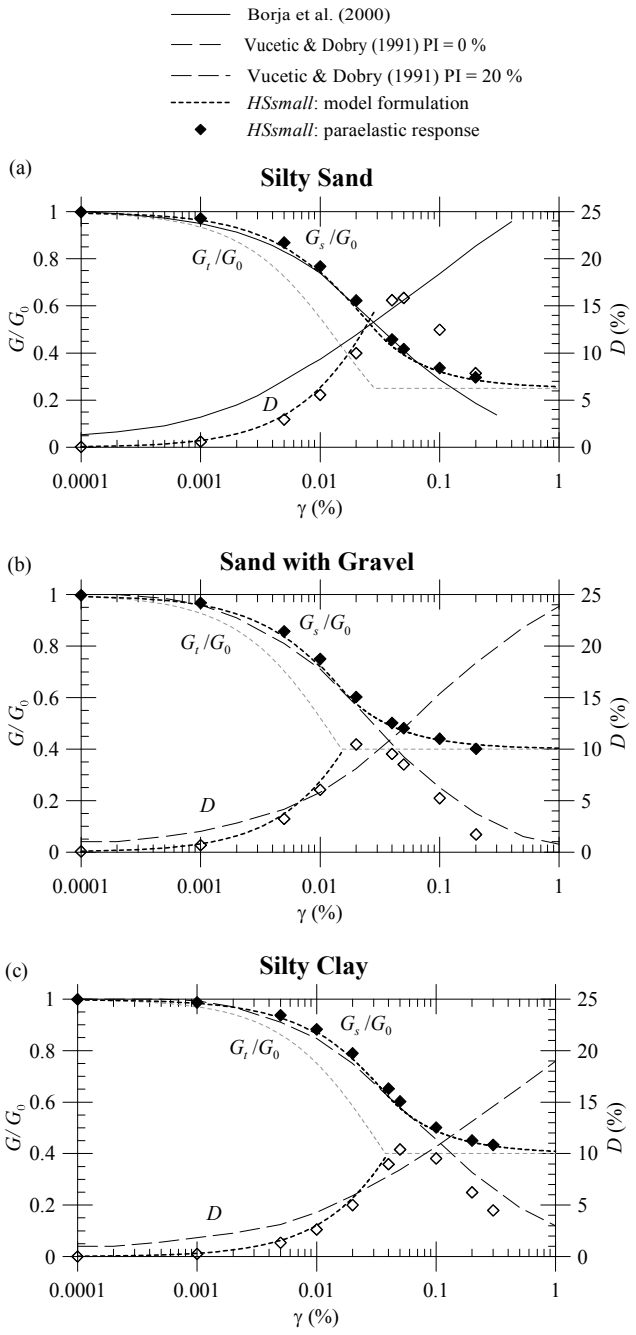
Borja et al. (2000)
Vucetic & Dobry (1991) PI = 0 %
Vucetic & Dobry (1991) PI = 20 %
HSsmall: model formulation
HSsmall: paraelastic response
(a)
Silty Sand
(b)
Sand with Gravel
(c)
Silty Clay
G/G0
D (%)
γ (%)
Gs/G0
Gt/G0
D
0.0001
0.001
0.01
0.1
1
0
0.2
0.4
0.6
0.8
5
10
15
20
25

Figure 9

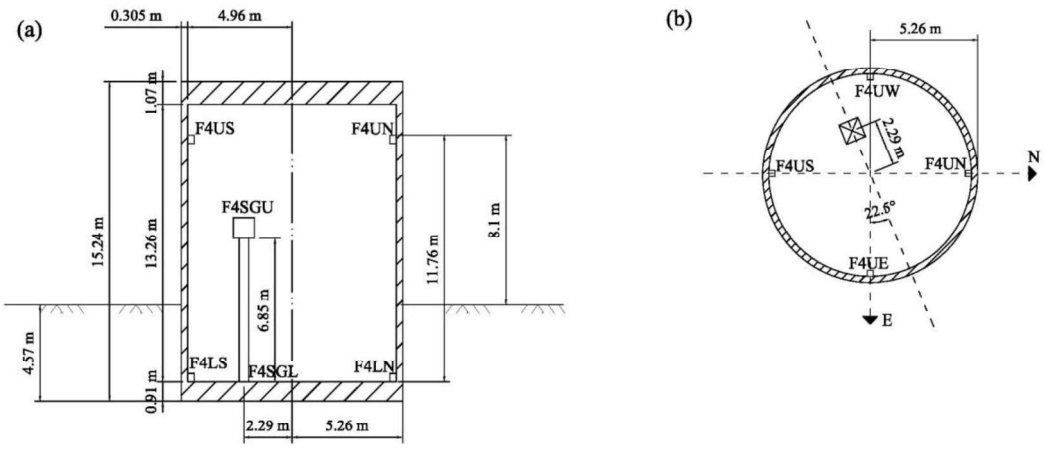
(a)
0.305 m
4.96 m
1.07 m
F4US
F4UN
F4SGU
15.24 m
13.26 m
8.1 m
11.76 m
6.85 m
4.57 m
F4LS
F4SGL
F4LN
0.91 m
2.29 m
5.26 m
(b)
5.26 m
F4UW
2.29 m
F4US
F4UN
N
22.5°
F4UE
E

Figure 10

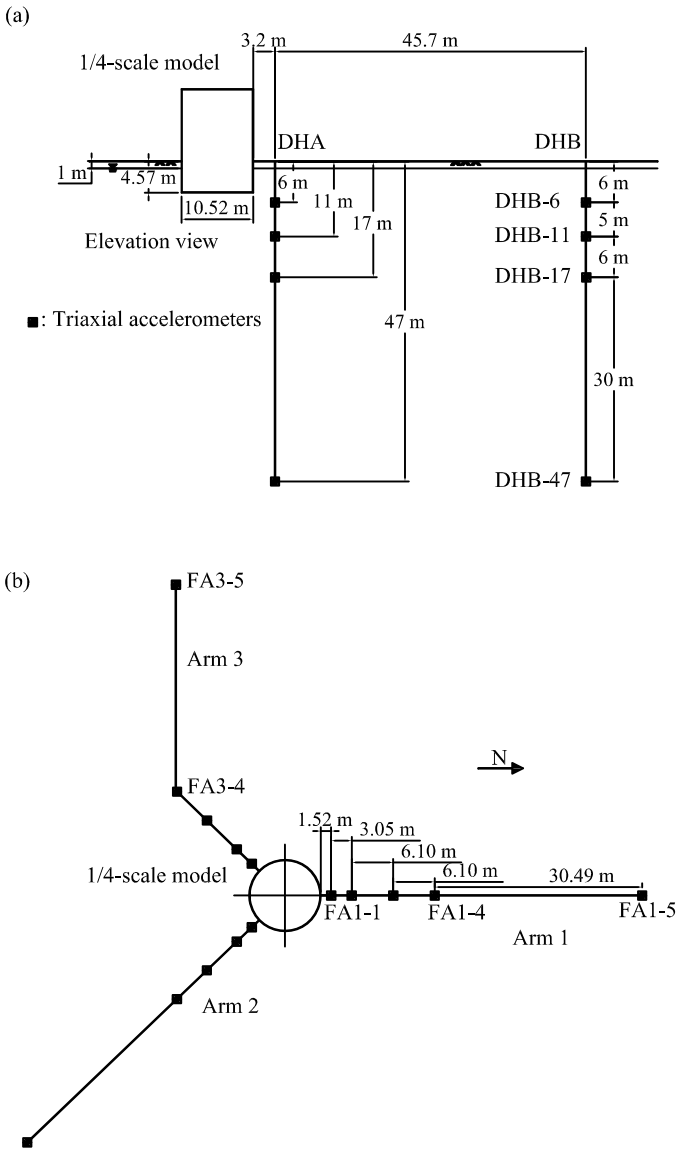
(a)
3.2 m
45.7 m
1/4-scale model
DHA
DHB
1 m
4.57 m
10.52 m
6 m
11 m
17 m
47 m
6 m
5 m
6 m
30 m
DHB-6
DHB-11
DHB-17
DHB-47
Elevation view
■: Triaxial accelerometers
(b)
FA3-5
Arm 3
FA3-4
N
1.52 m
3.05 m
6.10 m
6.10 m
30.49 m
1/4-scale model
FA1-1
FA1-4
FA1-5
Arm 1
Arm 2

Figure 11

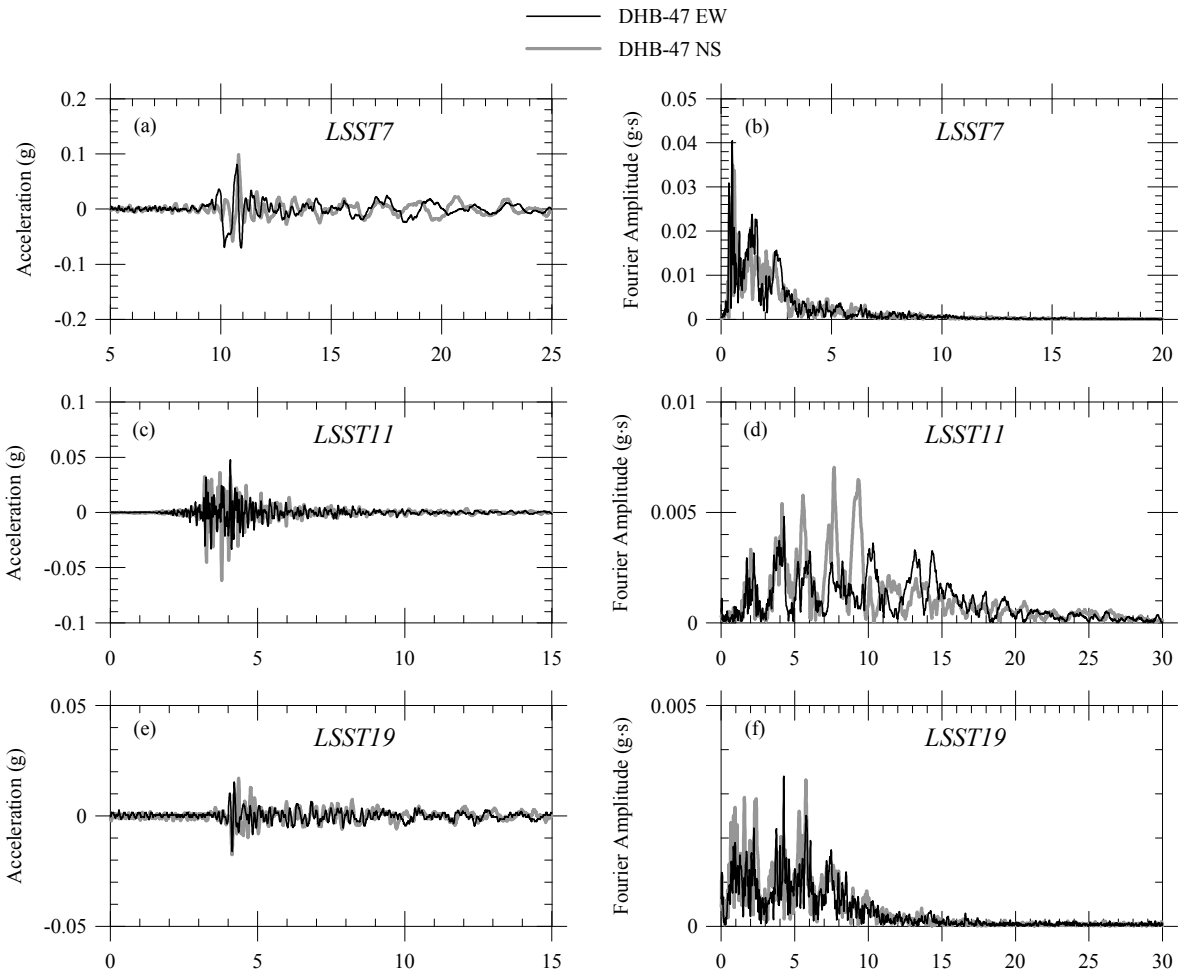
DHB-47 EW
DHB-47 NS
(a)
LSST7
Acceleration (g)
(b)
LSST7
Fourier Amplitude (g·s)
(c)
LSST11
Acceleration (g)
(d)
LSST11
Fourier Amplitude (g·s)
(e)
LSST19
Acceleration (g)
(f)
LSST19
Fourier Amplitude (g·s)

Figure 12

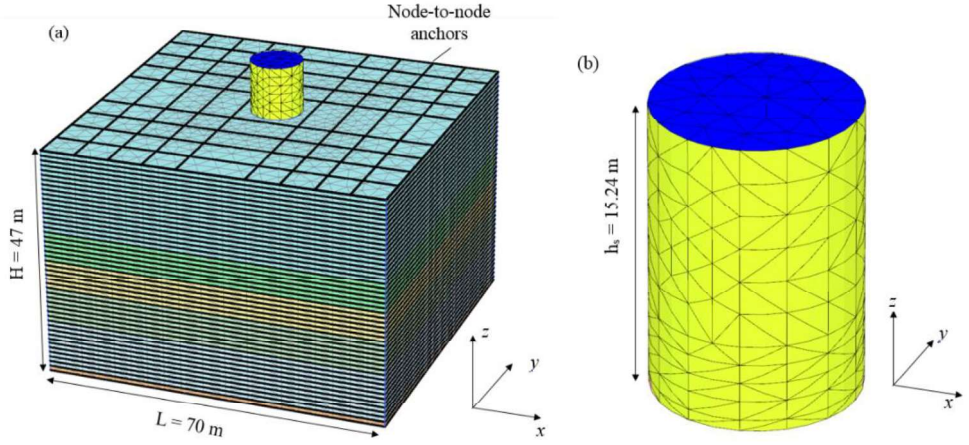

Figure 13

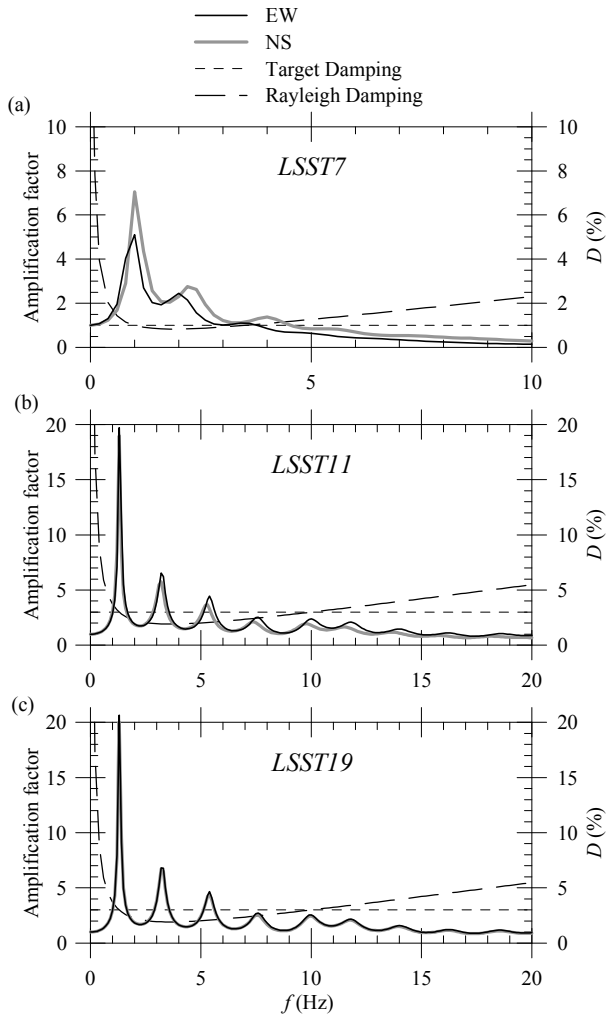
EW
NS
Target Damping
Rayleigh Damping
(a)
LSST7
(b)
LSST11
(c)
LSST19
Amplification factor
D (%)
f (Hz)

Figure 14

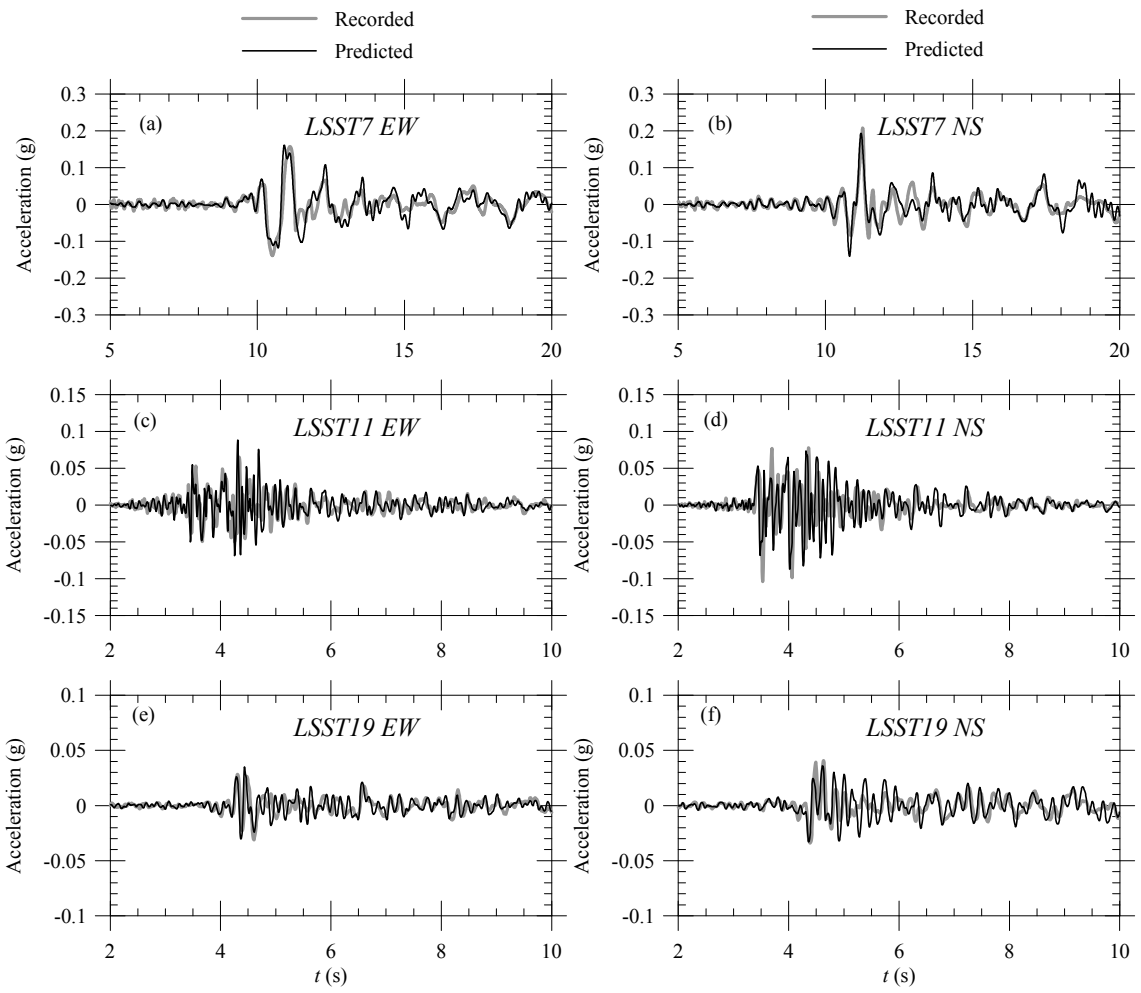
Recorded
Predicted
(a)
LSST7 EW
(b)
LSST7 NS
(c)
LSST11 EW
(d)
LSST11 NS
(e)
LSST19 EW
(f)
LSST19 NS
Acceleration (g)
t (s)

Figure 15

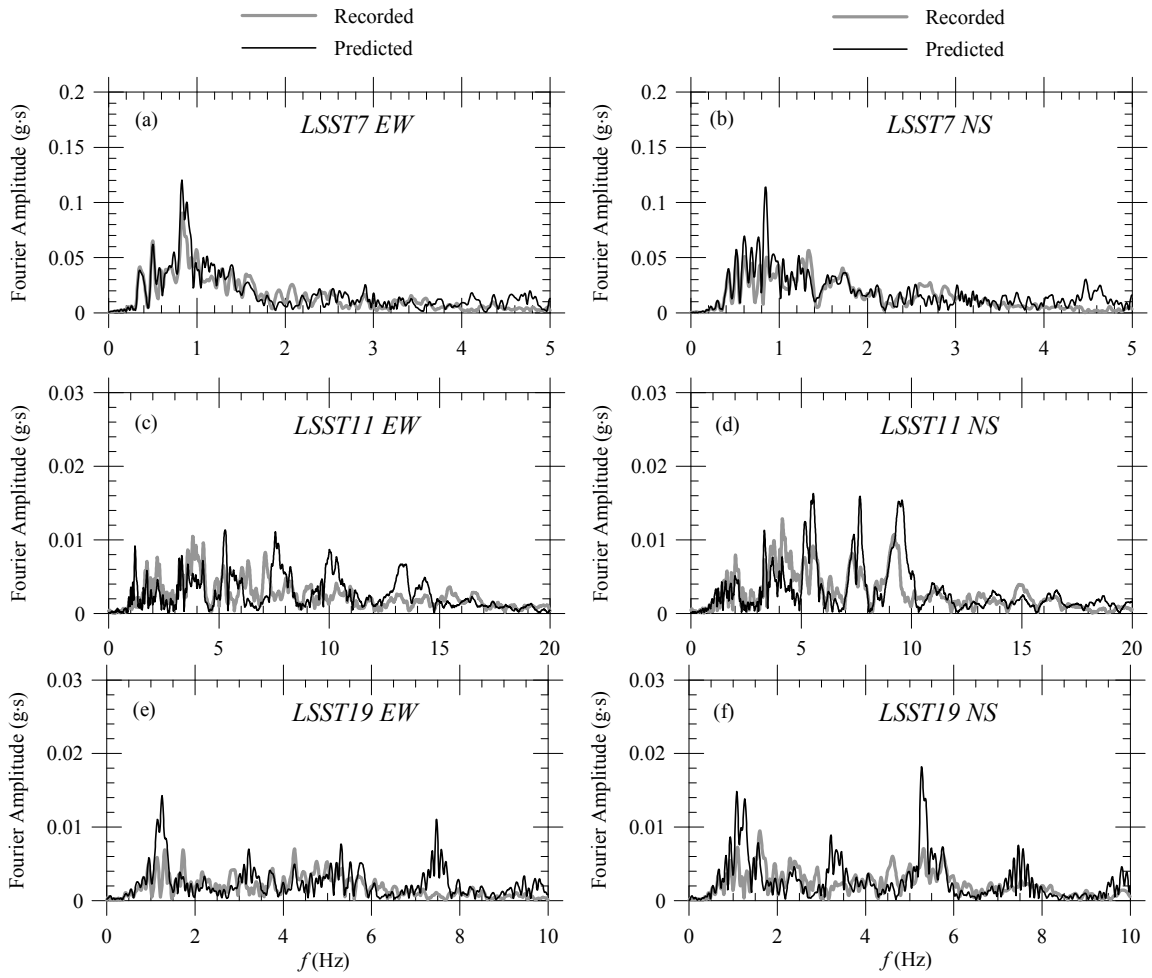
Recorded
Predicted
(a)
LSST7 EW
(b)
LSST7 NS
(c)
LSST11 EW
(d)
LSST11 NS
(e)
LSST19 EW
(f)
LSST19 NS
Fourier Amplitude (g·s)
f (Hz)

Figure 16

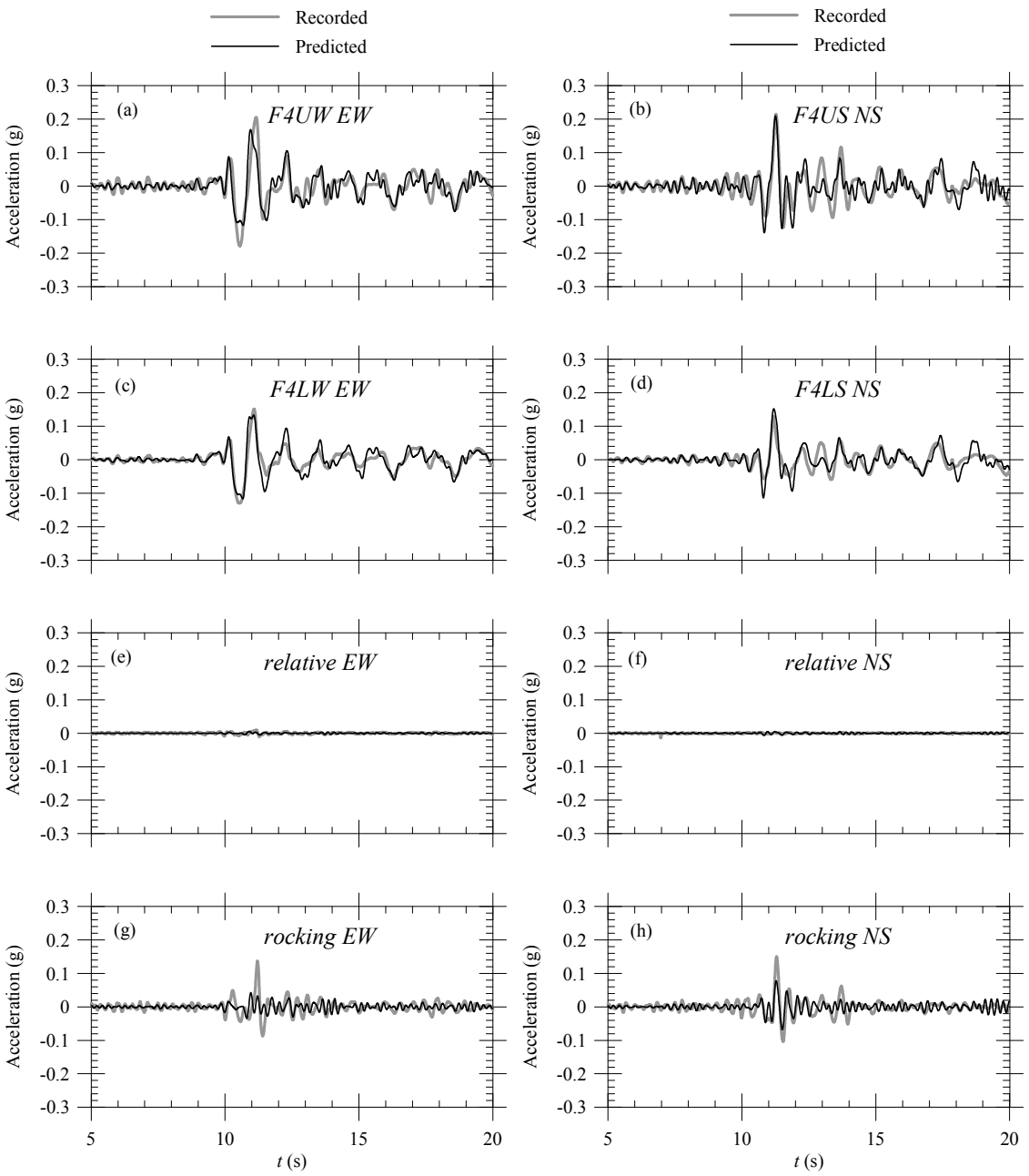
Recorded
Predicted
(a)
F4UW EW
(b)
F4US NS
(c)
F4LW EW
(d)
F4LS NS
(e)
relative EW
(f)
relative NS
(g)
rocking EW
(h)
rocking NS
Acceleration (g)
0.3
0.2
0.1
0
-0.1
-0.2
-0.3
5
10
15
20
t (s)

Figure 17

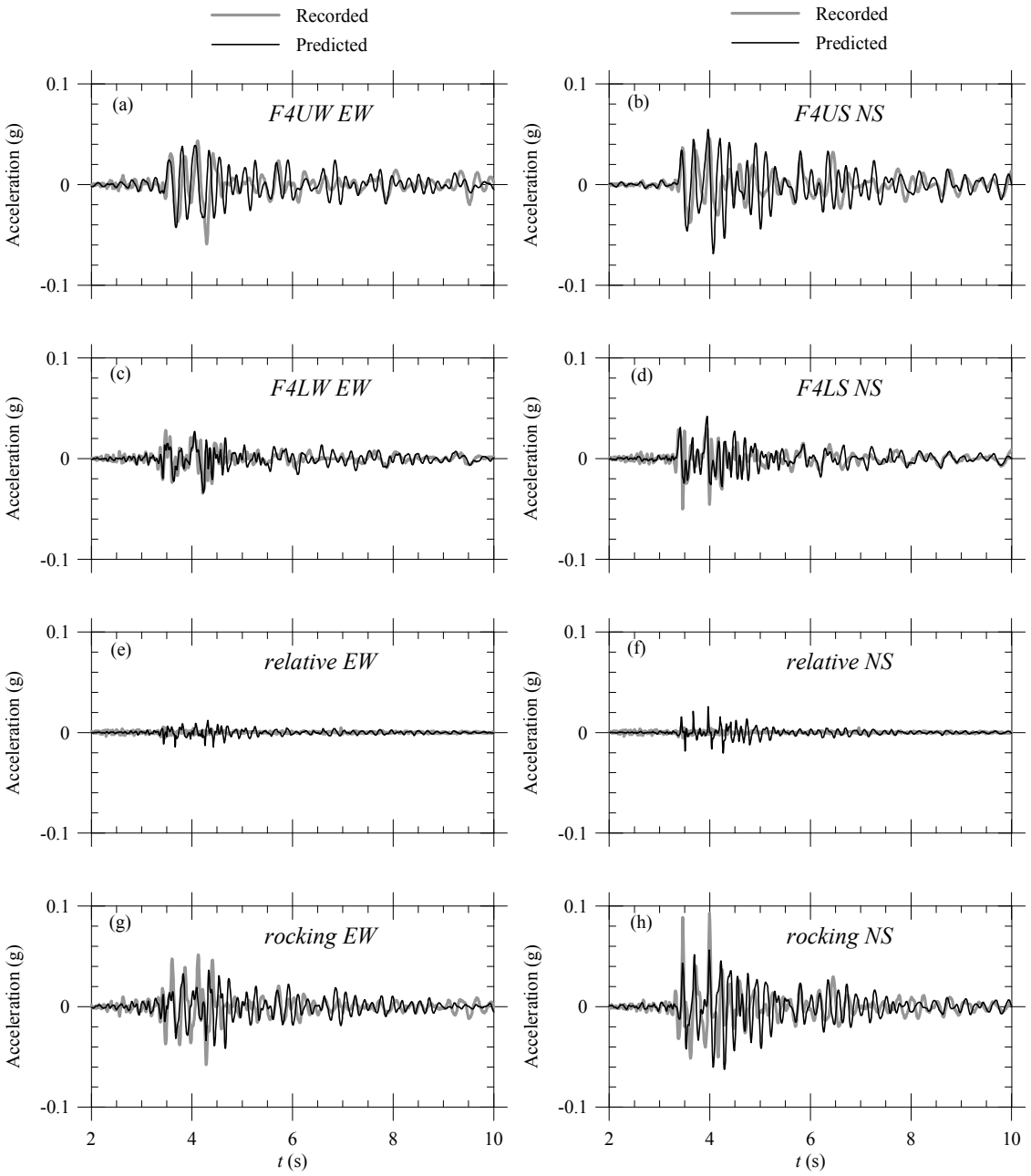
Recorded
Predicted
(a)
F4UW EW
(b)
F4US NS
(c)
F4LW EW
(d)
F4LS NS
(e)
relative EW
(f)
relative NS
(g)
rocking EW
(h)
rocking NS
Acceleration (g)
0.1
0
-0.1
2
4
6
8
10
t (s)

Figure 18

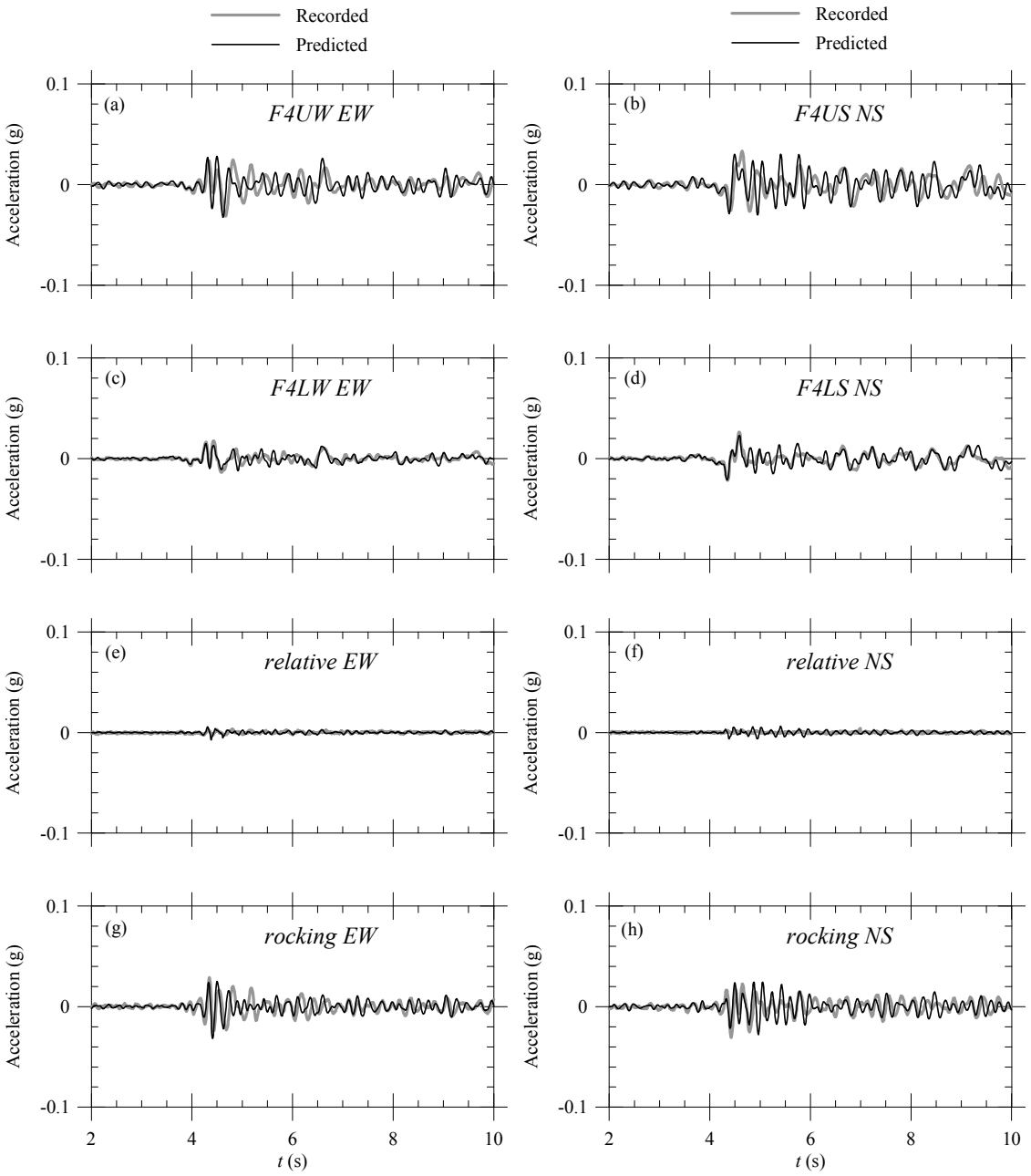
Recorded
Predicted
(a)
F4UW EW
(b)
F4US NS
(c)
F4LW EW
(d)
F4LS NS
(e)
relative EW
(f)
relative NS
(g)
rocking EW
(h)
rocking NS
Acceleration (g)
0.1
0
-0.1
2
4
6
8
10
t (s)

Figure 19

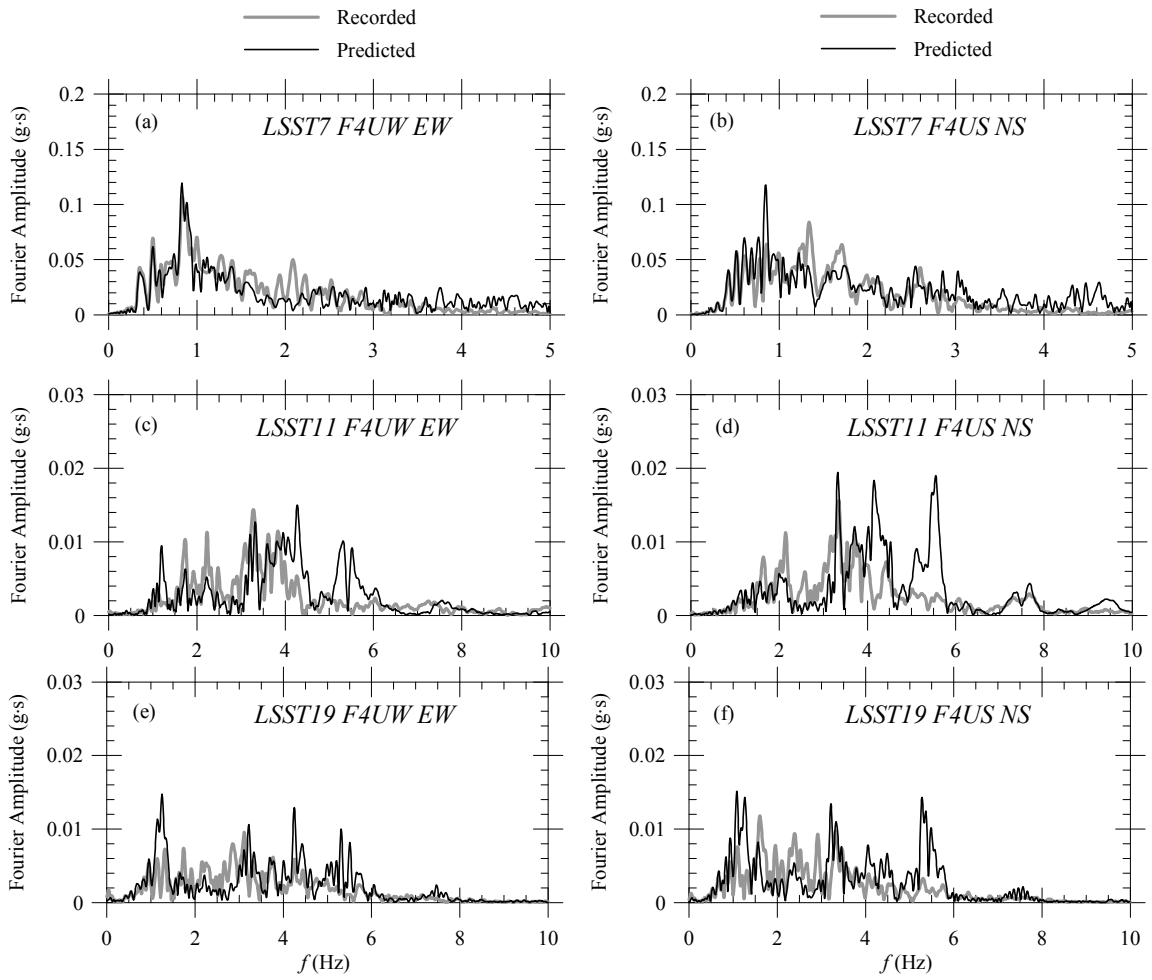
Recorded
Predicted
(a)
LSST7 F4UW EW
(b)
LSST7 F4US NS
(c)
LSST11 F4UW EW
(d)
LSST11 F4US NS
(e)
LSST19 F4UW EW
(f)
LSST19 F4US NS
Fourier Amplitude (g·s)
f (Hz)

Figure 20

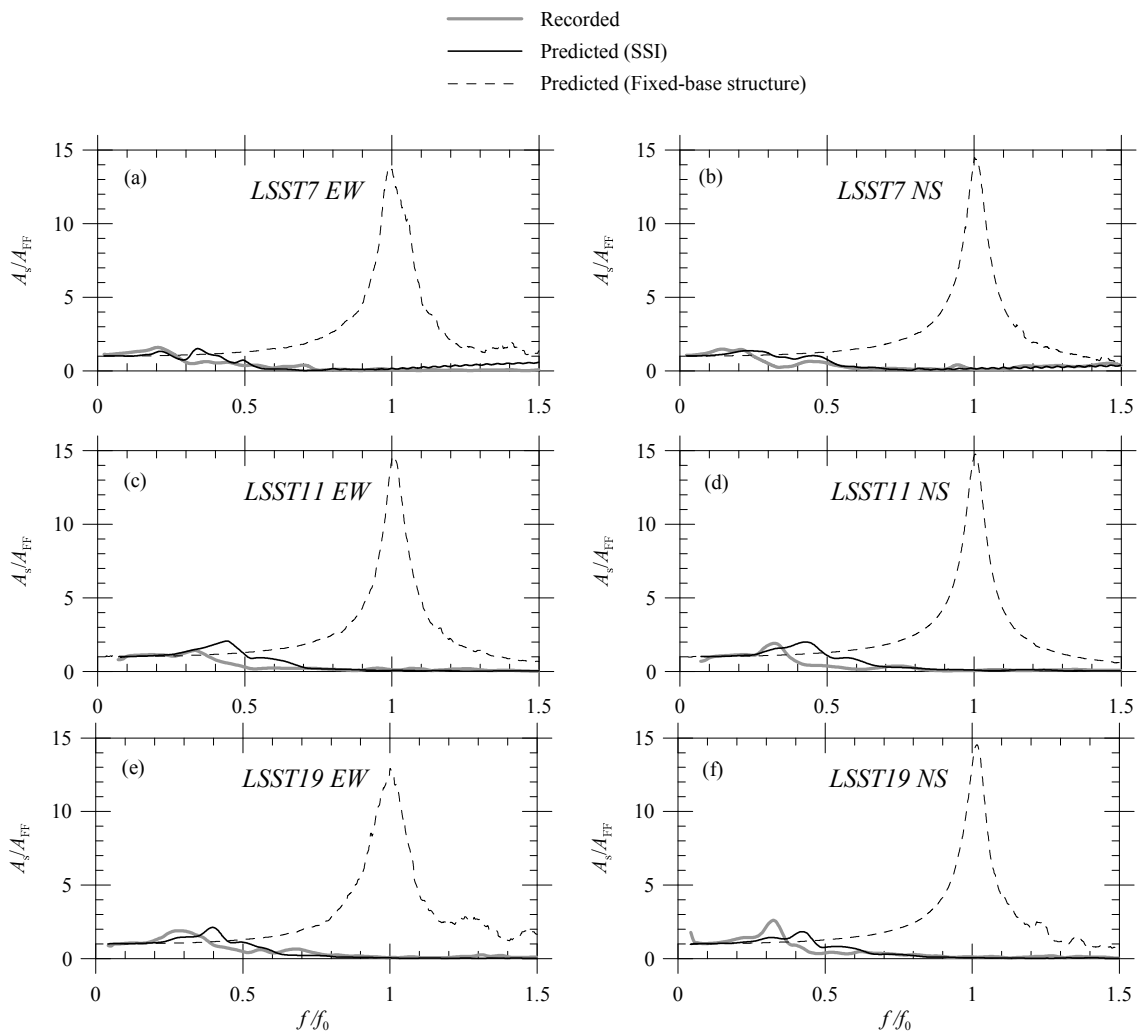
Recorded
Predicted (SSI)
Predicted (Fixed-base structure)
(a)
LSST7 EW
(b)
LSST7 NS
(c)
LSST11 EW
(d)
LSST11 NS
(e)
LSST19 EW
(f)
LSST19 NS
A_s/A_{FF}
f/f_0
0
5
10
15
0.5
1
1.5

Dynamic Soil-Structure Interaction: a three-dimensional numerical approach and its application to the Lotung case study

A. Amorosi*

Department of Structural and Geotechnical Engineering, Sapienza University of Rome, Italy

D. Boldini

Department of Civil, Chemical, Environmental and Materials Engineering, University of Bologna, Italy

A. di Lernia

Department of Civil, Environmental, Building Engineering and Chemistry, Technical University of Bari, Italy

Prof. Angelo Amorosi
Sapienza University of Rome
Department of Structural and Geotechnical Engineering
via Eudossiana 18, 00184 Rome, Italy
e-mail: angelo.amorosi@uniroma1.it
phone: 0039-06-44585982

Prof. Daniela Boldini
University of Bologna
Department of Civil, Chemical, Environmental and Materials Engineering
via Terracini 28, 40131 Bologna, Italy
e-mail: daniela.boldini@unibo.it
phone: 0039-051-2090233

Dr. Annamaria di Lernia
Technical University of Bari
Department of Civil, Environmental, Building Engineering and Chemistry
via Orabona 4, 70125 Bari, Italy
e-mail: annamaria.dilernia@poliba.it

* Corresponding Author

ABSTRACT

This paper presents a three-dimensional non-linear finite element (FE) approach to analyse the dynamic soil-structure interaction (SSI) phenomena observed at the Lotung Large-Scale Seismic Test (LSST) site. The numerical study is carried out in the time domain by a commercial FE code, taking into account the non-linear behaviour of soil and the multi-directional nature of real seismic events. The soil response is simulated by an isotropic hardening elasto-plastic hysteretic model (HSsmall) implemented in the material model library of the code. This model allows to describe the non-linear cyclic response ranging from small to large strain amplitudes and to account for the variation of the initial stiffness with depth.

In the paper, the FE numerical approach is first validated through a series of parametric analyses simulating simplified cases (i.e. linear visco-elastic structures founded on a homogeneous linear visco-elastic soil deposit) for which analytical solutions exist. Then, it is adopted to back-analyse the behaviour of the 1/4-scale nuclear power plant containment structure constructed at the Lotung LSST site which was shook by several earthquakes of different intensities and frequency contents. The FE results are thus compared to the recorded in-situ free-field and structural motions, highlighting the satisfactory performance of the numerical model in replicating the observed response. The overall outcome of this research proves that nowadays complex dynamic SSI phenomena can be tackled by direct approach, overpassing the strong simplifications of the well-established substructure approaches.

Keywords

Dynamic soil-structure interaction; seismic ground response; FE numerical modelling; direct method; Lotung LSST; multidirectional conditions.

1 Introduction

Most of the famous and devastating earthquakes, such as those occurred in Mexico (Mexico City, 1985), USA (Loma Prieta, 1989; Northridge, 1994) and Japan (Kobe, 1995), highlighted the important role played by soil-structure interaction phenomena on the dynamic response of surface structures [1]. It is thus well-recognised that the transient and permanent seismic-induced motion of structures is generally affected by the compliance of the soil-foundation system and it typically differs from that experienced by the same structure when supported by a rigid base (e.g. rock). The occurrence of a vibrating structure influencing the response of the soil and, at the same time, the ground motion affecting the response of the structure is referred to as dynamic Soil-Structure Interaction (SSI) [2,3].

The main consequence of SSI is the deviation of the motion at the base of the structure from that experienced by the soil at the same level under free-field conditions (i.e. in absence of structures). This difference is attributed to the simultaneous occurrence of two mechanisms dominating the SSI: the kinematic and the inertial interaction. The kinematic interaction, which is particularly relevant for embedded and piled foundations, arises because of the inability of a stiff foundation to follow the deformations that would occur in the soil, thus producing a deviation (usually a reduction) of the foundation motion from that of the ground under free-field conditions. The kinematic interaction induces an amplitude reduction of the translational component of motion at high frequencies and gives rise to rotational components [4–6]. The inertial interaction results from the development of inertial forces in the vibrating structure, associated to additional shear and bending excitation at the foundation level together with supplementary relative displacements between the foundation and the soil. This kind of interaction produces a variation of the dynamic properties of the structure-foundation system in terms of natural frequencies and associated damping ratio. In fact, the fundamental frequency of the system can be significantly decreased, depending on the relative stiffness of the structure and the soil, and the damping ratio is typically increased as a consequence of both wave radiation emanating from the foundation and soil dissipative capacity [6–12].

The role of SSI in the seismic response of structures founded on soft soil has traditionally been considered beneficial from a structural point of view, though in some cases it has been demonstrated to be detrimental, depending on the characteristics of seismic events [13,14].

In standard engineering practice, the evaluation of SSI effects is commonly performed adopting the so-called *substructure approach*, consisting in separately analysing the inertial and kinematic interaction mechanisms, often referring to analytical solutions available in the literature [4–9,11,15–20]. In this case the SSI analyses are typically carried out in the frequency domain, assuming a linear behaviour for both the structure and the soil.

In presence of strong earthquakes soil non-linearity should not be disregarded: at this scope, it is worth adopting a non-linear numerical approach in the time domain, by using the so-called *direct method*. This latter consists in modelling the entire soil-structure system in a single analysis [2]. Although a lot of

scientific effort has been put in the development of sophisticated methodologies to account for seismic SSI phenomena, the numerical analyses are frequently conducted under two dimensional plane strain conditions, assuming an equivalent-linear approach to account for the dynamic non-linear soil behaviour [21–25]. Nevertheless, more accurate and realistic solutions would ideally require the use of a three-dimensional numerical model combined to truly non-linear constitutive laws [26–29].

The contribution of this paper goes along this latter direction: a 3D Finite Element (FE) approach is adopted to investigate the seismic ground response and the dynamic soil-structure interaction problem in a unique analysis, accounting for the non-linearity and possible heterogeneity of a realistic soil deposit. The numerical model is set up by adopting the FE code PLAXIS 3D [30]. The non-linear soil behaviour under wave propagation processes is accounted for by an isotropic hardening elasto-plastic hysteretic model for the soil, named Hardening soil model with small strain stiffness (HSsmall). This constitutive model accounts for the non-linear behaviour of soil in the small strain range, which is particularly relevant in the seismic wave propagation problems, by means of a para-elastic hysteretic scheme based on a modified version of the Masing's rules, which is coupled to a distortional isotropic hardening plasticity model. In detail, it allows to take into account the variation of the initial stiffness with depth and the soil non-linearity, to mimic the shear modulus and damping ratio reduction curves [31–33]. The predictive capability of the HSsmall constitutive model in geotechnical earthquake engineering applications has recently been investigated [34–37]. In [37] the para-elastic response of the model has been examined in detail and validated at the single element level for both standard and multi-directional simple shear conditions. Furthermore, the back-prediction of the free-field seismic ground response as observed in a well-documented case history has been carried out, under both single-directional and multi-directional loading conditions, demonstrating the capability of the constitutive model in simulating wave propagation processes. The proposed 3D numerical approach has then been adopted to perform some preliminary investigations on its predictive capability with reference to proper SSI cases (i.e. in presence of a surface structure), limiting the analyses solely to single-directional conditions, i.e. only applying a single horizontal component of the selected input motion [38].

The present paper is aimed at extending this research programme, in order to tackle realistic 3D multi-directional SSI problems. As a first step, a preliminary parametric study of SSI phenomena is conducted by modelling simple linear visco-elastic structures, represented by single-degree-of-freedom (SDOF) structural models, founded on a linear visco-elastic soil medium. This is aimed at verifying the effectiveness of the approach in reproducing well established analytical results proposed in the literature for such simplified conditions. In particular, the analytical solutions proposed by Veletsos and co-workers [9,10] for surface foundations are adopted to assess the capability of the numerical model in replicating SSI effects and to explore in detail the impact of the inertial interaction phenomenon.

In the following sections, a more complex 3D non-linear FE model is developed to back-analyse the behaviour of the 1/4-scale model of a nuclear power plant containment structure set up at the Large-Scale Seismic Test site (LSST) in Lotung. This site experienced many seismic events, providing high quality

accelerometric data at different depths in the ground and on the model structure. In the following, reference will be made to the three earthquakes that shook the site in 1986, denoted as LSST7, LSST11 and LSST19.

A number of studies were conducted to investigate the free-field seismic ground response at Lotung site, highlighting the role of soil non-linearity and demonstrating the predictive capabilities of constitutive models and numerical codes [39–46]. Most of the soil-structure interaction analyses for that site were focused on the response of the structure as modelled by the substructure method, thus assuming an equivalent-linear approach to account for strain-dependent soil non-linearity [47–49]. With reference to the direct method approach, a 3D finite element approach was developed by Borja *et al.* [50] to study the effects of SSI on the ground motion recorded in the proximity of the containment structure, assuming for the soil behaviour an elasto-plastic constitutive model, but this did not include the structure itself in the numerical model.

In the present study the focus is on the dynamic response of both the structure and the soil deposit, as predicted by a unique model incorporating the containment structure and the soil. On site, the structural motion was monitored by accelerometers installed at the top and the bottom of the structure, while the free-field ground motion was recorded by a downhole array located sufficiently far away from the containment structure. The elasto-plastic hysteretic model HSsmall is here adopted to simulate the non-linear behaviour of soil, while a linear visco-elastic hypothesis is assumed for the structural model. The 3D numerical analyses are performed by simultaneously applying both horizontal components of each selected earthquake event as recorded by the accelerometer located at the larger depth along the instrumented downhole array.

2 Preliminary parametric SSI study

2.1 Analytical solution for inertial interaction

The inertial interaction mechanism is typically investigated by assimilating the structure to a simplified Single-Degree-Of-Freedom (SDOF) oscillator of height h and mass m_{str} supported by a rigid circular foundation resting on a homogeneous linearly elastic medium. In the analytical solutions proposed by Veletsos and co-workers [9,10] the soil compliance is represented by couples of springs and dashpots attached to the foundation element accounting for each mode of vibration (translational or rotational). Springs and dashpots are characterised by frequency-dependent dynamic impedance functions, expressed in the form:

$$k_j^* = k_j\left(a_0,\nu\right) + i\omega c_j\left(a_0,\nu\right) = K_j\left(\alpha_j + ia_0\beta_j\right) \tag{1}$$

where j denotes each mode of vibration, ω is the angular frequency of the input signal, a_0 is a dimensionless frequency parameter defined as $a_0 = \omega r/V_s$, r is the radius of the circular foundation, V_s is the soil shear wave velocity, ν is the soil Poisson's ratio, K_j is the static stiffness, k_j and c_j are the stiffness and damping coefficient of the springs and dashpots, dependent on the frequency through α_j and β_j; these latter are the dynamic impedance coefficients, whose approximate formulae are reported in [8] as a function of Poisson's ratio ν.

The static stiffness K_j depends on the soil stiffness and the geometry of the foundation. For a circular foundation lying on the surface of a halfspace, the translational K_u and rotational K_θ static stiffness are expressed as:

$$K_u = \frac{8Gr}{2-\nu}, \quad K_\theta = \frac{8Gr^3}{3(1-\nu)} \tag{2a,b}$$

where G is the soil shear stiffness modulus. Several analytical solutions are available in the literature for the determination of the impedance functions for rigid foundations of any geometry resting on the surface of a homogeneous halfspace (e.g. [7,8,51,52]).

Veletsos and co-workers [9,10] found that the fundamental frequency of the oscillator on a flexible-base f_e and the associated damping ratio ζ_e are related to the fixed-base dynamic properties of the structure by means of the following expressions:

$$\frac{f_e}{f_0} = \frac{1}{\sqrt{1+\frac{k}{k_u}+\frac{kh^2}{k_\theta}}} \tag{3}$$

$$\zeta_e = \zeta^* + \left(\frac{f_e}{f_0}\right)^3 \zeta_0 \tag{4}$$

where f_0 and ζ_0 are the fixed-base natural frequency and damping ratio of the structure founded on a rigid base respectively, and k is the stiffness of the fixed-base structure. The dynamic impedance coefficients α_j and β_j are evaluated for the flexible-base natural frequency f_e by an iterative procedure. ζ^* is referred to as foundation damping ratio and describes the dissipative capability of the soil-foundation system due to wave radiation and hysteretic soil damping, whose closed-form expression is reported in [9,10]. According to Eqs. (3) and (4) the SSI effects produce a reduction in the natural frequency of the flexible-base structure f_e with respect to that of the fixed-base structure f_0, due to the increased flexibility of the soil-foundation system, and a variation of the associated apparent damping ζ_e, which is a function of the frequency ratio f_e/f_0.

In order to describe the relationship between the dynamic behaviour of the flexible-base and the fixed-base structures, three dimensionless parameters are identified:

$$\underline{h} = \frac{h}{r} \tag{5}$$

$$\sigma = \frac{V_s}{f_0 h} \tag{6}$$

$$\gamma_m = \frac{m_{str}}{\rho \pi r^2 h} \tag{7}$$

where $\underline{h}$ is the slenderness ratio, σ is the soil-to-structure stiffness ratio and γ_m is the structure-to-soil mass ratio. This latter parameter is defined in terms of m_{str}, the mass of the structure, and ρ, the soil density. SSI effects depend on the dynamic properties of the supporting soil, the geometry and properties of the foundation element and the characteristics of the superstructure. In general, the frequency ratio f_e/f_0 decreases as the soil-to-structure stiffness ratio σ decreases and the slenderness ratio $\underline{h}$ increases. The apparent damping

ratio ζ_e becomes higher for decreasing values of σ and low values of the aspect ratio $\underline{h}$ (i.e for squatty structures), while it reduces for high values of $\underline{h}$ (i.e for slender structures). In general, the SSI effects are more pronounced for relatively stiff structures lying on relatively soft soils.

In the present work, a preliminary parametric study is carried out by changing one-by-one the above-mentioned dimensionless parameters, with the aim of giving an insight on the impact of each of them on SSI phenomena and of validating the proposed numerical approach by performing a comparison between analytical solutions and FE results.

2.2 Description of the numerical model

The soil-structure interaction problem is analysed for vertically propagating shear waves in the time domain employing the Finite Element code PLAXIS 3D [30]. The analyses are carried out with reference to SDOF structures located at the ground surface of a 50 m thick idealised soil deposit. This latter is assumed as homogenous and linear visco-elastic, consistently with the analytical solutions. It is characterised by a shear wave velocity V_s constant with depth and equal to 126 m/s, damping ratio D_{soil} equal to 5 %, unit weight of 18 kN/m^3 and Poisson's ratio ν of 0.33.

The acceleration time history recorded at Tarcento (Friuli, Italy) during the earthquake occurred in 1976 is adopted as input motion. The original seismic signal is characterised by a magnitude equal to 5.3, a duration of 16.85 s and peak ground acceleration equal to 0.21 g. The input signal is scaled to a peak ground acceleration of 0.35 g and filtered to prevent frequencies higher than 12 Hz (Fig. 1), aiming at limiting the finite element dimension adopted in the mesh. The signal is applied at the bottom of the soil deposit along one horizontal direction, consistently with what assumed in the analytical formulation adopted here as a reference [9].

The SDOF structures are modelled as 3D single-storey building frames, in which four columns are schematised as massless *beam* elements of stiffness k_{beam} (equal to ¼ of the stiffness k of the whole structure), overtopped by a rigid *plate* element (E = 10^{11} MPa) of mass m_{str} (Fig. 2). To avoid relative displacements among the nodes at the roof of the structure, additional *beam* elements of similar stiffness are introduced along the perimeter of the *plate* element. All the adopted structural elements are modelled as linear visco-elastic. The oscillators are supported by a rigid (E = 10^{11} MPa) and massless surface footing of circular shape, having a radius r of 3 m and unit thickness. Consistently with the hypotheses the analytical solution is based on, perfect bond is assumed between the foundation element and the supporting soil, i.e. no interface elements are used, such that any relative displacement between the structure and the soil (e.g. uplifting or sliding) is neglected.

The geometric characteristics of the structural elements of the oscillator are determined through the following procedure:

- given the soil shear wave velocity V_s and assumed the slenderness ratio $\underline{h}$, the soil-to-structure stiffness ratio σ and the foundation dimension (the radius r), it is straightforward to deduce the fixed-base natural frequency f_0 of the SDOF structure from Eq. 6;

- assuming a value for the structure-to-soil mass ratio γ_m, the mass m_{str} is obtained from Eq. 7 and assigned, in terms of unit weight γ_{str}, to the square-shaped *plate* element of length l equal to 3 m and thickness equal to 1 m;
- the stiffness of the fixed-base structure k could then be determined through the following equation:

$$f_0 = \frac{1}{2\pi}\sqrt{\frac{k}{m_{str}}} \tag{8}$$

- the size of the square section of each column is estimated as a function of the moment of inertia J, assumed equal in both directions of translation, with reference to the stiffness of 3D single-storey building frames given by:

$$k = \frac{12nEJ}{h^3} \tag{9}$$

where $n = 4$ is the number of columns and E is the Young's modulus of the structural material, here assumed equal to $2.5 \cdot 10^4$ MPa, a typical value for concrete.

The structural damping ratio ζ_0 is assigned to the weightless columns through the simplified Rayleigh formulation [53], which considers the damping matrix as a function of the stiffness matrix only:

$$[C] = \beta_R [K] \tag{10}$$

where the Rayleigh coefficient β_R is defined as:

$$\beta_R = \frac{2D^*}{\omega^*} \tag{11}$$

The control angular frequency ω^* is selected equal to the fixed-base natural angular frequency ω_0 of the SDOF structure, while the target damping ratio D^* is taken equal to the structural damping ratio $\zeta_0 = 2.5$ %.

The dissipative capacity of the soil is also introduced in the analyses by the frequency-dependent viscous damping of the full Rayleigh formulation. According to this latter the damping matrix is a linear combination of the mass [M] and stiffness [K] matrices of the system:

$$[C] = \alpha_R [M] + \beta_R [K] \tag{12}$$

Rayleigh coefficients α_R and β_R are obtained as a function of the target damping ratio D^* according to:

$$\begin{Bmatrix} \alpha_R \\ \beta_R \end{Bmatrix} = \frac{2D^*}{\omega_m + \omega_n} \begin{Bmatrix} \omega_m \omega_n \\ 1 \end{Bmatrix} \tag{13}$$

The angular frequencies ω_m and ω_n are related to the frequencies f_m and f_n, defining the interval over which the viscous damping is equal to or lower than the damping ratio D^*, assumed herein equal to $D_{soil} = 5\%$. The selection of the frequencies requires a suitable strategy of calibration, such as that proposed by Amorosi *et al.* [54], according to which the first Rayleigh frequency f_m is identified as the first natural frequency of the soil deposit excited by the input motion, while the second frequency f_n is selected as that at which the amplification function gets lower than one. Such procedure requires a preliminary equivalent linear visco-elastic analysis, typically performed by 1D codes (EERA in this case [55]).

In Fig. 3 the amplification function of the selected input signal is depicted together with the corresponding Rayleigh damping curve and the target damping ratio. According to the adopted calibration strategy, values

of 0.6 Hz and 7 Hz are selected for f_m and f_n, respectively, corresponding to $\alpha_R = 0.3472$ and $\beta_R = 0.00209$, considered constant with depth.

Three series of parametric analyses are performed, simulating SDOF structures characterised by different dimensionless parameters, selected with the aim of highlighting some peculiar aspects of the SSI effects. Thus, for the purpose of investigating the influence of soil-to-structure stiffness ratio σ, four oscillators are modelled by keeping constant the slenderness ratio $\underline{h}$ (equal to 1) and the structure-to-soil mass ratio γ_m (equal to 0.16) and varying the soil-to-structure stiffness ratio σ, here assumed equal to 4, 5, 10 and 15. In order to inspect the influence of the slenderness ratio $\underline{h}$, three different values (1, 3 and 5) are adopted in the structural modelling, keeping fixed the ratio σ to 5 and 10, while the structure-to-soil mass ratio γ_m is set as before. Finally, aiming at studying the effects of the structural mass, the SDOF properties are modified consistently with a structure-to-soil mass ratio γ_m equal to 1.43, keeping the slenderness ratio $\underline{h}$ equal to 1 and exploring the soil-to-structure stiffness ratio σ in the range 4-15. The dynamic properties of the fixed-base SDOF models, determined by means of the above procedure, are summarised in Tables 1 and 2, with reference to each series of parametric analyses.

The peculiar behaviour of the soil-structure system founded on a compliant soil deposit is here highlighted by comparing it with the performance of the same structure founded on a rigid soil deposit. As such for each oscillator defined above, dynamic analyses are also performed considering the soil as infinitely rigid. This condition is achieved by assigning to the soil a Young's modulus E equal to 10^{11} MPa.

The employed mesh is characterised by a width along each horizontal direction equal to the thickness of the soil deposit (Fig. 4). The domain is discretised in 43935 10-node tetrahedral elements and is partitioned into 50 horizontal layers of unit thickness, to ensure the maximum average dimension of the element being lower than one-eighth of the wavelength associated with the maximum frequency component f_{max} of the input wave.

During the static stages the boundary conditions are the standard ones, i.e. total fixities to the nodes at the bottom of the mesh, while nodes on the lateral sides are allowed to move solely along the vertical direction. For the dynamic stages, the bottom of the mesh is assumed as rigid and prescribed displacements are applied along one horizontal direction (i.e. the x-axis); *tied nodes* boundary conditions [56] are assumed, consisting in connecting nodes on the corresponding vertical sides to constrain them to move horizontally by the same quantity, while vertical displacements are forbidden. This condition is achieved by manually introducing horizontal node-to-node anchor elements, characterised by high axial stiffness EA (equal to 10^9 kN), which connect nodes at the same depths on the opposite lateral sides of the domain. Related to this modification of the horizontal constraints is the unavoidable perturbation of the static stress equilibrium, which is restored by introducing pressures corresponding to the lithostatic distribution of horizontal effective stresses on the vertical sides of the model. This latter precaution is strictly necessary when a stress-dependent constitutive model is used. The lateral vertical sides of normal y are allowed to displace freely in the horizontal x direction and clamped in both y and z directions, thus ensuring that the system is only excited along one lateral direction.

All the analyses are carried out performing an initial static stage, during which the construction of the structure is simulated, followed by the dynamic stage, when the seismic signal is applied at the bottom of the mesh. No water level is considered in the numerical analyses, that are performed under drained conditions.

The standard Newmark solution method is adopted during the dynamic stages, with parameters $\alpha_N = 0.25$ and $\beta_N = 0.05$, ensuring the stability of the algorithm while not providing any numerical damping [54,57]. This latter aspect is relevant in this set of analyses as they are aimed at reproducing the analytical solutions in which, by definition, no additional damping is included.

2.3 Numerical results

The dynamic response of the SDOF models is typically presented in terms of amplification function, defined as the ratio of the acceleration Fourier amplitude A_s of a specific node at the top of the structure (representing the motion of the structure) to the acceleration Fourier amplitude of the free field motion A_{FF} recorded at the ground surface (i.e. in absence of structures), plotted against the frequency f normalised with respect to the fixed-base natural frequency f_0 (Fig. 5). The amplification function A_s/A_{FF} is introduced to identify the natural frequency of the soil-structure system, while its maximum amplitude $(A_s/A_{FF})_{max}$ provides a measure of the damping ratio associated to the soil-structure system, according to the relationship $\zeta = 1/[2(A_s/A_{FF})_{max}]$[2].

With reference to the first series of parametric analyses, in which oscillators are characterised by $\gamma_m = 0.16$ and $\underline{h} = 1$, for decreasing values of σ the natural frequency of the soil-structure system f_e results more and more shifted to lower values as compared to the fundamental one of the fixed-base structure f_0 (Fig. 5a-c). Furthermore, the associated apparent damping ratio ζ_e increases, as shown by the reduction of the peak amplitude of the amplification function of the flexible-base structures. In general, the smaller the soil-to-structure stiffness ratio σ the more pronounced the above SSI effects. On the contrary, for increasing soil-to-structure stiffness ratio σ, the soil-foundation compliance has a limited influence on the dynamic response of the structure, which tends to behave as a fixed-base one (Fig. 5c).

The change in apparent damping is normally beneficial for short and squatty structures, subjected to a reduction in the amplitude of the motion, but it could be detrimental for tall and slender ones, whose predominant mode of vibration is the rocking one, characterised by a significantly lower radiation damping and by an increase in the maximum amplitude of the amplification factor $(A_s/A_{FF})_{max}$. This aspect is accurately captured by the FE models, as shown in Fig. 5d and e, where the amplification functions exhibit an increment in the peak amplitude corresponding to the resonant frequency as the slenderness ratio $\underline{h}$ increases. With reference to the model characterised by $\underline{h}$ equal to 5, the magnitude of the amplification function increases of about 60% indicating a significant reduction in the apparent damping ratio ζ_e as compared to the structural one ζ_0.

The frequency ratios f_e/f_0 and the apparent damping ζ_e, obtained by analytical solutions for $\gamma_m = 0.16$ and $\underline{h} = 1$, are plotted against the soil-to-structure stiffness ratio σ in Fig. 6a and b together with those obtained by the numerical analyses; the variation of f_e/f_0 and ζ_e with σ for the case of $\gamma_m = 1.43$ is also depicted in the

same plots. A representation of the dependence of the frequency ratio f_e/f_0 and the apparent damping ratio ζ_e on the slenderness ratio $\underline{h}$ is shown for $\gamma_m = 0.16$ in Fig. 6c and d.

A fairly good agreement between FE simulation results and analytical solutions is obtained, demonstrating the effectiveness of the proposed numerical model for simulating the SSI phenomena. For all the analysed cases both the SSI fundamental frequency normalised to the fixed-base structure natural frequency f_e/f_0 and the apparent damping ratio are well reproduced numerically. For high slenderness ratios $\underline{h}$ (i.e. 3 and 5), this latter ratio exhibits lower values than the structural one ζ_0 (i.e. less than 2.5%), particularly for low soil-to-structure stiffness ratio σ (Fig. 6d).

For massive structures ($\gamma_m = 1.43$), the SSI effects are more appreciable in terms of reduction in the fundamental frequency of the soil-structure system; however, at low soil-to-structure stiffness ratio σ (less than 5), the apparent damping ratios for heavy structures are significantly lower than those observed for light ones (i.e. $\gamma_m = 0.16$). This behaviour is ascribed to the development of higher inertial forces, caused by the rotation of the foundation system, which reduce the contribution of the radiation effect on the overall damping ratio.

3 The case study: dynamic soil-structure interaction at Lotung

The above simulations illustrate the effectiveness of the adopted numerical approach in solving idealised soil-structure interaction problems. Under more complex hypotheses, i.e. real three-dimensional configuration, soil non-linearity and heterogeneity, for which the analytical solutions are no longer representative, the direct approach represents a convenient option. Such an approach is thus adopted here to back-analyse the structural and ground seismic responses recorded at the Large Scale Seismic Test (LSST) site in Lotung.

3.1 Description of the Large Scale Seismic Test site

The Large-Scale Seismic Test (LSST) was a joint research programme, established in 1985 between the U.S. Electric Power Research Institute (EPRI) and the Taiwan Power Company (TPC), for the purpose of studying the effects of soil-structure interaction on the response of a nuclear power plant containment structure [49]. Under the LSST project, two scaled-down reinforced concrete models (1/4 and 1/12 scales) of a nuclear power plant containment structure were built in Lotung, a highly seismic region in the North-East of Taiwan. The larger of the two small-scale structures and the surrounding area were extensively instrumented to record both the structural and ground seismic responses during earthquakes that shook the area, providing an excellent database for studying the site effects and understanding the SSI phenomena. Indeed, SSI effects were found to have a considerable influence on the seismic response of the monitored structures, due to their very high stiffness and mass and to the local relatively soft soil conditions.

The LSST site is placed on the Lanyang River plain, which is underlain by two layers of recent alluvium and Pleistocene deposits resting on a Miocene basement at about 400 m below the ground surface. The local geological profile at the LSST site is characterised by a layer of silty sand extending down from the surface

to a depth of 17 m, overlying a 6 m thick layer of sand with gravel. Underneath the sand layer, a stratum of silty clay extends down to the maximum investigated depth of 47 m and is interlayered by an inclusion of sand with gravel between 29 m and 36 m of depth (Fig. 7a). Groundwater level is detected at about 1 m below the ground surface and the related pore pressure distribution is hydrostatic.

The geotechnical characterisation of the soil deposit is based on the available in-situ tests and the back-analyses of seismic data found in the literature [39,41,58,59]. The strength properties of coarse-grained soils are determined by SPT tests (Fig. 7b), using the interpretation approach proposed by De Mello [60]. Thus, for the silty sand material a frictional angle φ' of 30° is assumed, while the sand with gravel layers are characterised by φ' equal to 35° and 37° at 17-23 m and at 29-36 m, respectively. For the silty clay soil, typical mechanical properties are adopted, i.e. cohesion c' equal to 10 kPa and frictional angle φ' equal to 24°. A total unit weight of 19.6 kN/m^3 is assumed as an average value for the entire deposit [58].

The shear wave velocity profile is obtained by cross-hole tests [58,59], executed in the area down to 47 m, as depicted in Fig. 7c. The distribution of V_s with depth points out the soft nature of the soil deposit, as it varies from about 100 m/s at the ground surface to 300 m/s at 47 m depth.

With reference to the upper layer of silty sand (0 – 17 m) (Fig. 8a), the decay curves of normalised secant shear modulus, G_s/G_0, and damping ratio D are those obtained by Zeghal *et al*. [39], through a back-interpretation of in-situ recorded ground response. The shear modulus and damping ratio decay curves, evaluated at the depth of 11 m, are assumed as representative of the entire silty sand layer, as reported by Borja *et al*. [41]. Due to the lack of specific experimental data, typical decay curves proposed in the literature are assumed for the other soil layers (Fig. 8b, c). In particular, the curves suggested by Vucetic & Dobry [61] for plasticity index PI equal to 0 % and 20 % are selected for coarse-grained and silty soil layers, respectively.

The 1/4-scale nuclear power plant containment model was a reinforced concrete cylindrical shell structure of external radius of 10.52 m, as shown in Fig. 9a. The total height of the structure was 15.24 m, of which 4.57 m embedded into the soil below the ground surface. The cylindrical structure was characterised by a constant thickness of 0.305 m, while the roof slab and the basement slab were 1.07 m and 0.91 m thick, respectively. Within the containment structure, a steel shell structure was built for simulating a steam generator prototype of a nuclear power plant; this latter was resting on the basement of the containment structure at about 2.3 m far from the axis of the cylindrical structure (Fig. 9b).

3.2 Monitoring data

The layout of the LSST site instrumentation is depicted in Fig. 10. It consisted in surface accelerometric arrays, located along three equally spaced arms (FA1, FA2 and FA3), which extend radially from the 1/4-scale structural model, and two downhole arrays, arranged at about 3 m (DHA) and 49 m (DHB) from the edge of the same structural model along Arm 1. Both the surface and the downhole arrays contained triaxial accelerometers oriented in the East-West (EW), North-South (NS) and vertical directions.

The surface accelerometers were located at distances of 1.52 m, 4.57 m, 10.67 m, 16.77 m and 47.26 m from the edge of the 1/4-scale model, while the downhole arrays recorded the seismic ground motion at the depths

of 6 m, 11 m, 17 m and 47 m from the ground level. Due to its vicinity to the scaled-down containment structure, the soil response recorded by DHA array is expected to be affected by the structural seismic motion, while DHB recorded motion might be considered as under free-field conditions.

The 1/4-scale model was located in the centre of the radiating arms; it was consistently instrumented in order to monitor its dynamic response (Fig. 9). This instrumentation included four accelerometers installed on the roof (F4U) and four others on the basement (F4L), along EW and NS diametrical direction. Two additional accelerometers were located at the top (F4SGU) and the bottom (F4SGL) of the inner steam generator prototype.

The non-linear FE numerical investigations are conducted with reference to three seismic events, selected based on their different characteristics, such as peak accelerations, time durations and frequency content bandwidths. In particular, the simulations are performed adopting the acceleration time histories recorded during the seismic events of May 20th 1986 (denoted as LSST7 event), of July 17th 1986 (LSST11 event) and of December 8th 1986 (LSST19 event), whose characteristics are summarised in Table 3. The acceleration time histories along both EW and NS horizontal directions, recorded at the largest depth by the accelerometer DHB-47 (Figs. 11), are assumed as rigid bedrock motions in the numerical analyses. The LSST7 event (Fig. 11a) might be identified as a strong motion and characterised by a low frequency content, this similarly to the LSST19 event (Fig. 11c), which, on the contrary, represents a weak motion. The LSST11 seismic event (Fig. 11b) is classified as a weak motion and is characterised by a high frequency content and a low peak ground acceleration.

4 Numerical model of LSST case study

4.1 Finite element discretisation

The back-predictions of the dynamic response of the soil deposit and of the containment structure are carried out in the time domain, applying simultaneously both the horizontal components of the input ground motion recorded at the depth of 47 m (DHB-47), assumed here as the bedrock. For the sake of simplicity in this study the effects of the vertical component are not addressed, although in some cases they might be non-negligible, as recently discussed in [62].

The employed mesh is characterised by a height of 47 m (equal to the depth of the investigated soil deposit) and a width of 70 m along each horizontal direction (about 7 times the diameter of the containment structure), in order to include the 1/4-scale structural model in the numerical domain and avoid any boundary effect on the structural response (Fig. 12a). The soil deposit is discretised by 91648 10-noded tetrahedral elements and vertically subdivided in 47 unit horizontal layers, aiming at optimising the element dimension. For this reason, a low-pass filter at 20 Hz is applied to the input motions, together with a baseline correction, this latter in order to avoid the fictitious accumulation of displacements at the end of the seismic event.

The boundary conditions for the static stages are the customary ones, as described in Section 2.2. During the dynamic stage, the previously discussed *tied nodes* approach is adopted. Both EW and NS horizontal components of each selected input motion are simultaneously prescribed at the base of the numerical model.

The nuclear power plant containment structure (Fig. 12b) is modelled by linear visco-elastic plates, characterised by typical values of reinforced concrete materials, i.e. unit weight $\gamma_{concrete}$ of 25 kN/m^3, Young's modulus E equal to $2.53 \cdot 10^4$ MPa and Poisson's ratio ν of 0.2. Due to the lack of direct information, a 2.5% of structural damping ratio ζ_0 is assigned to the *plate* elements by means of the simplified Rayleigh formulation (Eq. 10). According to Eq. 11, the Rayleigh coefficient β_R is determined as a function of the target damping ratio (assumed equal to 2.5%) and the control angular frequency ω^*, selected equal to 10 Hz, i.e. a value that approximates the natural frequency of the fixed-base containment structure. For the sake of simplicity, no interface elements are introduced in the model, given the lack of experimental information on the soil-structure contact conditions.

The FE analyses are carried out performing one static stage, in which the construction of the containment structure is considered, followed by a dynamic stage simulating the occurrence of the earthquake event. A time step *dt* equal to 0.005 s is assumed according to the requirement suggested by Bathe [63]. All dynamic analyses are performed assuming fully undrained conditions.

The selected Newmark time integration parameters are $\alpha_N = 0.3025$ and $\beta_N = 0.6$. These parameters for the examined problem and for the adopted time step lead to a small amount of numerical damping which filters any spurious high-frequency oscillations [e.g. 64].

4.2 The *HSsmall* soil constitutive model

4.2.1 Model description

The non-linear behaviour of soil is described by the HSsmall model, available in the material library of the adopted FE code. [30]. This model is based on the well-known Hardening Soil model (*HS*) [31], extended by the elastic small strain overlay formulation proposed by Benz [32,33]. It belongs to the class of the isotropic hardening elasto-plastic models and allows to describe the non-linear behaviour of soil even at very small strain levels by means of a para-elastic hysteretic formulation inspired by the Masing's rules. In the model formulation, the Authors [32,33] introduced a scalar strain history-dependent value, denoted as γ_{Hist}, which accounts for any variation in the strain increment direction and memorises the deviatoric strain history of the material. The scalar strain amplitudes are related to material shear stiffness through a modified version of the simple hyperbolic law proposed by Hardin-Drnevich [65]:

$$\frac{G_s}{G_0} = \frac{1}{1 + 0.385 \frac{\gamma_{Hist}}{\gamma_{0.7}}} \tag{14}$$

where $\gamma_{0.7}$ represents the shear strain level at which the secant shear modulus G_s is reduced to about 70% of the initial shear modulus G_0. The tangent shear stiffness modulus G_t is evaluated through the following expression:

$$G_t = \frac{G_0}{\left(1 + 0.385 \cdot \frac{\gamma_{Hist}}{\gamma_{0.7}}\right)^2} \geq G_{ur} = \frac{E_{ur}}{2(1+\nu_{ur})} \tag{15}$$

It is bounded by a lower cut-off value, corresponding to the elastic unloading-reloading shear stiffness G_{ur}, expressed as a function of the Poisson ratio ν_{ur} and the unloading-reloading modulus E_{ur}. Through the strain value γ_{Hist}, a unique value of tangent stiffness is evaluated, which describes the stress-strain relationship along all directions in a multi-axial loading condition.

As soon as the shear strain level exceeds the cut-off shear strain $\gamma_{\text{cut-off}}$:

$$\gamma_{cut-off} = \frac{\gamma_{0.7}}{0.385}\left(\sqrt{\frac{G_0}{G_{ur}}} - 1\right) \tag{16}$$

the tangent shear stiffness modulus G_t becomes constant and equal to G_{ur}.

Under cyclic loading conditions, the hysteretic soil behaviour mimics the modified Masing'rules [66], providing hysteresis loops that account for the energy dissipation and leading to a hysteretic damping ratio defined as the ratio of dissipated energy to maximum strain energy [67]. It is worth highlighting that the damping ratio curve is theoretically characterised by decreasing values tending asymptotically to zero for shear strain amplitudes larger than $\gamma_{cut-off}$; in fact, at that stage the loops become narrower as a consequence of the constant tangent shear stiffness $G_t = G_{ur}$. Consequently, beyond the threshold strain limit $\gamma_{cut-off}$, the secant shear stiffness modulus G_s decreases asymptotically towards the unloading-reloading tangent stiffness modulus G_{ur},. In Fig.8 the normalized secant shear modulus and the damping ratio curves are depicted as obtained by the model formulation (dashed curves) and the numerical simulation (symbols). It is worth remarking that this latter behaviour refers to the pre-yield paraelastic response of the model, used in the calibration of the corresponding model parameters. However, upon yielding irreversible strains become predominant, leading to a decrease of the shear modulus and to the corresponding increase of the damping ratio, resunting in an overall evolution of the behaviour with shear strain amplitude more similar to what experimentally observed in soils.

The initial shear modulus G_0 is described as a function of the effective stress and strength parameters c' and φ' according to the following relationship (Eq. 17)

$$G_0 = G_0^{ref}\left(\frac{c' \cdot cos\,\varphi' + \sigma_3' \cdot sin\varphi'}{c' \cdot cos\,\varphi' + p^{ref} \cdot sin\varphi'}\right)^m \tag{17}$$

where G_0^{ref} is the reference initial shear modulus, defined as the value of G_0 at the reference confining pressure p^{ref} (here assumed as equal to the default value of 100 kPa), m is a constant depending on the soil type and σ_3' is the minor principal effective stress. Similar expressions govern the secant stiffness in standard drained triaxial test E_{50}, the unloading-reloading modulus E_{ur} and the tangent stiffness for primary oedometer loading condition E_{oed}.

The elastic domain of the constitutive model is bounded by a shear hardening yield surface, which can expand up to the Mohr-Coulomb failure criterion as a function of the deviatoric plastic strains, and a cap

yield surface, introduced to limit the elastic region for compressive stress paths. For the shear hardening yield surface a non-associated flow rule is employed, while an associated type is adopted for the cap yield surface.

4.2.2 Calibration of model parameters

With reference to the data available for the Lotung LSST site, the model parameters (Table 4) are determined according to a suitable procedure of calibration. As already discussed in [37], the reference initial shear modulus G_0^{ref} and the parameter *m* are selected in order to best fit the shear wave velocity profile, as shown in Fig. 7c. The strain parameter $\gamma_{0.7}$ is chosen to give the best approximation of the normalised shear modulus G_s/G_0 (Eq. 14) and damping ratio *D* decay curves, as depicted in Figs. 8. The elastic unloading-reloading shear stiffness modulus G_{ur}^{ref} is evaluated such that the ratio G_0^{ref}/G_{ur}^{ref} results equal to 4 for the silty sand layer and to 2.5 for the other soil layers, leading to fixed values for the $\gamma_{cut\text{-}off}$. The other stiffness parameters E_{50}^{ref} and E_{oed}^{ref} are assumed to be three times lower than the elastic unloading-reloading stiffness modulus E_{ur}^{ref}, determined as a function of G_{ur}^{ref} and the Poisson's ratio ν_{ur}, this latter assumed equal to 0.3 for coarse-grained soils [68] and to 0.25 for the silty clay material.

Earth coefficients at rest at normally consolidated states K_0^{nc} are calculated by the well-known Jâky's expression [69] for coarse-grained soils, while the modified expression for overconsolidated soils is adopted for fine-grained materials.

For the silty sand and sand with gravel soil layers, the overconsolidation ratio *OCR* is fictitiously set to 10, in order to avoid the activation of the cap surface included in the constitutive model, not necessary for the Lotung site deposits.

The failure ratio R_f, defined as the ratio of the ultimate deviatoric stress and the asymptotic value of the shear strength, was considered equal to the standard value 0.9.

As the model predicts null values of damping ratio at very small strain level, it is required to add a small amount of it (typically in the order of 1-3%, see Fig. 8) by the Rayleigh formulation [53], as discussed in section 2.2.

In Figs. 13 the amplification functions obtained by preliminary equivalent-linear analyses performed by EERA [55] with reference to both horizontal components (EW and NS) of the considered input motions are depicted together with the corresponding Rayleigh damping curves and the target damping ratio D^*. This latter is assumed equal to 1 % for the more intense event (LSST7), while a target damping D^* equal to 3 % is introduced in the LSST11 and LSST19 analyses, in order to provide an appropriate amount of viscous damping consistent with the average small strain level induced during weak motions [37]. With reference to the weak motions LSST11 and LSST19, the amplification functions for each horizontal direction are very similar, while they slightly differ for the more intense LSST7 event, where non-linearity plays a major role in the response.

Concerning the LSST7 earthquake (Fig. 13a), the calibration strategy leads to the selection of f_m equal to 1 Hz and f_n equal to 3.5 Hz, considering the amplification function relative to EW component of motion, which provides a lower value of the second control frequency as compared to that of the NS component. As far as the LSST11 (Fig. 13b) and LSST19 (Fig. 13c) events concerns, the first control frequency f_m is assumed equal to the fundamental frequency of the soil deposit, i.e. 1.3 Hz, while the second one f_n is selected equal to 10 Hz, approximately corresponding to the average value of the first and second crossing of the amplification factor with the unity value.

5 Numerical results and comparison with monitoring data

In the following a surface node at a sufficiently large distance from the containment structure and nodes placed on top and at the basement of the structural model are selected.

The containment structure is characterised by high stiffness, thus the horizontal components of the seismic motion recorded by the four accelerometers placed on its top, and similarly for those at the bottom of the construction, are equal to each other. As such, F4UW and F4LW accelerometers are considered representative of the structural response along EW direction, while F4US and F4LS accelerometers are selected to monitor the motion along NS one.

5.1 Seismic ground response

Figs. 14 and 15 illustrate the numerically predicted and in-situ recorded motion at ground surface (FA1-5) during the three earthquakes. The results, plotted in terms of acceleration time history and Fourier spectra along the two horizontal directions EW and NS, should be considered as only marginally influenced by the structure, as such being representative of "free-field" conditions.

With reference to the more intense seismic signal LSST7, it emerges that the observed response is well-reproduced, both in terms of peak acceleration and zero crossings (Fig. 14a, b). The overall frequency content of the signal is also satisfactory back-calculated by the model. Nevertheless, a slight over-prediction of the soil motion amplitudes might be recognised, related to the tendency of the model to mobilise a reduced amount of damping at large strain levels under multi-directional shear conditions [37]. In fact, in such conditions the soil response appears to be characterised by thinner shear stress-strain hysteresis loops. Related to this feature is the generation of significant numerical noise at high frequencies, which is attenuated using a low-pass filter (cut-off frequency of 5 Hz) applied to the numerical results (Fig. 15a, b).

As far as the LSST11 earthquake concerns (Fig. 14c, d and Fig. 15c, d), the computed response is similar to the in-situ one, particularly for the NS component. The overall frequency content is well captured by the model, although a slight overestimation of the Fourier amplitudes for some specific frequencies is observed.

A similar pattern is also shown for the LSST 19 case (Fig. 14e, f and Fig. 15e, f). The acceleration time histories at ground surface are similar to the recorded data, especially for the EW component. Nevertheless, the Fourier spectra highlight a slight over-estimation of the amplitudes around 1 Hz and 7.5 Hz, while the overall frequency content is reasonably well reproduced.

Given the complexity of the analyses, which include events characterised by rather different intensity, it can be concluded that the numerical tool is capable of reproducing the main features of the observed "free-field" responses, provided that a careful calibration of the model parameters is properly carried out.

5.2 Dynamic response of the 1/4-scale containment structure

The monitored motion at the basement of the structure differs from that experienced by the soil at the same depth under free-field conditions, due to soil-structure interaction phenomena which also trigger a non-negligible rocking component of motion. Thus, the dynamic response at the roof (F4U) of the 1/4-scale containment structure can be decomposed into three parts: the response at the base of the structure (F4L), the rocking motion and the deformation of the structure, all contributing to the response recorded at the top of it.

The rocking component of motion is evaluated by the same procedure for both the monitored and numerically obtained data: it is obtained multiplying the height of the structure by the rocking angle at the basement. This latter is computed as the ratio of the difference between the vertical motions, expressed in terms of accelerations at diametrically opposite accelerometers or corresponding nodes (e.g. F4LW and F4LE in the EW direction) and the distance between the two selected points. The deformation of the construction is estimated as the difference between the overall motion of the structure, recorded at its top, and the sum of the basement and the horizontal motions induced by the basement rotation.

The numerically predicted and the in-situ recorded motion at the roof of the containment structure and its decoupled components are depicted in Figs. 16-18 in terms of acceleration time histories along each horizontal direction for the LSST7, LSST11 and LSST19 earthquakes. It is worth highlighting that the SSI response of the containment structure is dominated by rocking, while the relative motion has a far lower impact on the overall response of the system. This is not surprising as the containment structure is rather rigid and massive while being founded on a relatively flexible soil deposit.

With reference to the more intense LSST7 earthquake, it appears that the dynamic motion predicted at the top of the numerical model matches fairly well that recorded at F4UW along EW direction and F4US for the NS direction (Fig. 16a, b). This is particularly true in this latter case, where the peak acceleration and zero crossings are accurately caught by the numerical model, while a slight underestimation of the peak acceleration is detected along the EW direction. The computed response at the basement of the 1/4-scale model is similar to the recorded one along both horizontal directions (F4LW EW and F4LS NS), in terms of peak acceleration and zero crossings (Fig. 16c, d). Furthermore, the predicted rocking component is characterised by lower amplitudes as compared to the recorded one (Fig. 16g, h), especially in EW direction, while the predicted relative motion is characterised by small amplitudes in accordance with the recorded data (Fig. 16e, f). It is worth recalling that, for the sake of simplicity, no vertical acceleration components were included in the numerical analyses, although they were recorded in situ. Nevertheless, for what concerns the rocking mode results, no major differences are detected between the numerical data and the observed ones.

A similar pattern is detected when the LSST11 event is considered (Fig. 17). In this case, the computed relative response is characterised by higher amplitudes, while a better estimation of the rotational motion is observed along the EW direction.

A satisfactory comparison between numerical prediction and recorded motion is also observed for the weaker motion LSST19 (Fig. 18).

Fig. 19 shows the above results for the roof of the containment structure in terms of Fourier spectra along both horizontal directions for the three investigated events. The overall frequency content is reasonably well captured by the numerical analyses. In detail, for the more intense LSST7 event, a slight overestimation of the amplitudes can be identified around 0.85 Hz along both horizontal directions. A similar pattern is observed for the LSST11 in the frequency range 4-6 Hz, while it emerges in the ranges of 1-1.5 Hz and 5-6 Hz for the LSST19 earthquake.

To highlight the SSI effects it is worth introducing the transfer function $H(\omega)$, defined as the ratio of the Fourier spectrum amplitude of the horizontal motion of the roof to that of the horizontal free-field ground response. This transfer function might not be defined throughout the whole frequency range, as the denominator might attain very small (sometimes zero) amplitudes at some frequencies, due to noise. As such, it seems more appropriate to refer to power spectral density functions (S_{input}, S_{output}) and cross spectral density ones ($S_{input\text{-}output}$) of the input and output signals, which always exhibit non-null amplitudes [70]:

$$H(\omega) = \frac{S_{output}}{S_{input-output}} \tag{18}$$

The transfer functions defined above are computed for the back-predicted and recorded responses. They are plotted in Fig. 20 against the frequency f normalised with respect to the fixed-base natural frequency of the structure. In the same figure the transfer function of the fixed-base structure is represented, i.e. that of the structure on a rigid base, so that the fixed-base fundamental frequency of the containment structure is also represented.

As expected, the compliance of the soil deposit induces a significant reduction of the fundamental frequency of the interacting system from that of the fixed-base structure. A corresponding increase of the damping ratio is also triggered by the SSI, associated to the augmented energy dissipation due to radiation and material damping: this feature leads to the significant reduction of the peak of the function shown in the figure.

While the numerical estimation of the dynamic response of the interacting system matches reasonably well the in-situ one in terms of associated damping ratio, a worst performance characterises the back-prediction of the natural frequency of the system. In fact, for the LSST7 seismic event the EW numerically predicted frequency ratio f_e/f_0 is about 0.32 while the measured one is equal to 0.2; similarly, in the NS direction the peak of the transfer function is at a frequency ratio f_e/f_0 equal to 0.22 instead of 0.14. This is also true for the less intense events, where the predicted frequency ratios f_e/f_0 attain larger values than the measured ones. This systematic discrepancy should be related to the poor information available about the structural properties of the containment model, which are particularly scarce with reference to its dynamic behaviour. In all the analyses proposed in this paper the structure is modelled based on the few data available, without adopting any iterative procedure to back-calibrate the model based on the numerical results.

6 Conclusions

In this paper a non-linear finite element approach is proposed for back-predicting the free-field ground response and the dynamic motion of a 1/4-scale model of a nuclear power plant containment structure, as recorded at Lotung Large-Scale Seismic Test site, in Taiwan, during three events characterised by different intensities and frequency contents. The numerical analyses were performed by a commercial 3D FE code capable of simulating the multi-directional wave propagation process under 3D conditions.

Aiming at validating the 3D numerical approach, a parametric study is first presented to illustrate the predictive capability of the FE model under simplified conditions for which analytical solutions are available in the literature. At this stage the effects of soil-structure interaction of a linear visco-elastic SDOF structure founded on a homogeneous visco-elastic soil medium are analysed. The numerical results are in fair agreement with the analytical solutions, both in terms of flexible-base natural frequency and associated damping ratio. As expected a consistent decrease of the natural frequency and increase of the damping ratio of the soil-structure system with respect to the fixed-base ones were recognised.

After this validation stage, the 3D numerical approach was adopted to back-analyse the seismic ground motion and the soil-structure interaction phenomena as recorded at Lotung LSST site. In these analyses the non-linear soil behaviour is described by a isotropic hardening elasto-plastic constitutive model which had already proved to be amenable for seismic ground response problems. The model accounts for the hysteretic non-linear behaviour at very small strain level by means of a Masing's rule-based para-elastic formulation. The calibration of the model parameters was performed straightforwardly based on the available shear modulus decay curves and shear wave velocity profile. The structural behaviour of the small-scale containment model was represented by a simple linear visco-elastic model, based on the few available information.

Time domain numerical analyses were performed under multidirectional condition of the seismic motion, i.e. simultaneously applying both horizontal components of the DHB-47 motion, recorded at the depth of 47 m from the ground surface.

The overall results of the FE numerical analyses proved to be in good agreement with both free field measurements recorded at the ground surface and structural monitoring data. Each component of the decoupled response of the roof, namely the rotational one associated to the inertial interaction effects, the deformation of the structure and the motion at the basement, were satisfactorily reproduced.

Furthermore, the main features of the dynamic structural response were also captured by the numerical simulations, both in terms of reduction of natural frequency of the interacting system with respect to the fixed-base one and of increase of associated damping ratio.

The promising performance of the proposed integral approach, which includes the soil and the structure in a unified model, supports the idea that in the next future the classical sub-structure schemes, where the above elements are separately analysed in a decupled way, might be overcome. In fact, although those simplified procedures appear more handable and easy to use, they are based on a number of strong simplifications (i.e. free-field seismic site response, linear spring and dashpots to mimic the soil in the structural analysis, linear

superposition of the results, fully decoupled behaviour, etc.) that might lead to rather inaccurate predictions under realistic site conditions, especially for those cases where multi-directionality and non-linearity are relevant. The robustness of numerical approaches, as the one discussed here, should always be verified against both available solutions under simplified conditions and in situ observations. Those latter seem to play a crucial role in the evolution of this research field and should be more and more supported by the scientific and technical communities in order to allow a proper step forward in this field.

References

[1] Hashash YMA, Phillips C, Groholski DR. Recent advances in non-linear site response analysis. Fifth Int. Conf. Recent Adv. Geotech. Earthq. Eng. Soil Dyn. Symp. Honor Profr. I.M. Idriss, San Diego, California: 2010.

[2] Kramer S. Geotechnical earthquake engineering. Upper Saddle River, N.J.: Prentice Hall; 1996.

[3] Kramer S, Stewart JP. Geotechnical Aspects of Seismic Hazards. Earthq. Eng. From Eng. Seismol. to Performance-Based Eng., CRC Press; 2004, p. 107.

[4] Elsabee F, Morray JP. Dynamic Behavior of Embedded Foundations. Massachusetts Institute of Technology, Department of Civil Engineering, Constructed Facilities Division; 1977.

[5] Day SM. Seismic response of embedded foundations. ASCE Conv., Chicago: 1978.

[6] Mylonakis G, Nikolaou S, Gazetas G. Footings under seismic loading: Analysis and design issues with emphasis on bridge foundations. Soil Dyn Earthq Eng 2006;26:824–53.

[7] Veletsos A, Wei Y. Lateral and rocking vibration of footings. ASCE J Soil Mech Found Div 1971;97:1227–48.

[8] Veletsos AS, Verbic B. Vibration of viscoelastic foundations. Earthq Eng Struct Dyn 1973;2:87–102.

[9] Veletsos AS, Meek JW. Dynamic behaviour of building-foundation systems. Earthq Eng Struct Dyn 1974;3:121–38.

[10] Veletsos AS, Nair VD. Seismic interaction of structures on hysteretic foundations. ASCE J Struct Div 1975;101:109–29.

[11] Bielak J. Dynamic behaviour of structures with embedded foundations. Earthq Eng Struct Dyn 1975;3:259–74.

[12] Wolf JP. Dynamic soil-structure interaction. Englewood Cliffs, NJ: Prentice Hall; 1985.

[13] Mylonakis G, Gazetas G. Seismic soil-structure interaction: Beneficial or detrimental? J Earthq Eng 2000;4:277–301.

[14] Jeremić B, Kunnath S, Xiong F. Influence of soil–foundation–structure interaction on seismic response of the I-880 viaduct. Eng Struct 2004;26:391–402. doi:10.1016/j.engstruct.2003.10.011.

[15] Veletsos AS, Prasad AM, Wu WH. Transfer functions for rigid rectangular foundations. Earthq Eng Struct Dyn 1997;26:5–17. doi:10.1002/(SICI)1096-9845(199701)26:1<5::AID-EQE619>3.0.CO;2-X.

[16] Kim S, Stewart JP. Kinematic Soil-Structure Interaction from Strong Motion Recordings. J Geotech Geoenvironmental Eng 2003;129:323–35.

[17] Jennings PC, Bielak J. Dynamics of building-soil interaction. Bull Seismol Soc Am 1973;63:9–48.

[18] Wong HL, Luco JE. Tables of impedance functions for square foundations on layered media. Int J Soil Dyn Earthq Eng 1985;4:64–81. doi:10.1016/0261-7277(85)90002-6.

[19] Dobry R, Gazetas G. Dynamic Response of Arbitrarily Shaped Foundations. J Geotech Eng 1986;112:109–35. doi:10.1061/(ASCE)0733-9410(1986)112:2(109).

[20] Gazetas G, Mylonakis G. Seismic soil-structure interaction: New evidence and emerging issues. Geotech Spec Publ 1998:1119–74.

[21] Lysmer J, Udaka T, Tsai CF, Seed HB. Flush- A computer program for approximate 3D analyis of soil-structure interaction problems 1975.

[22] Luco JE, Wong HL. Soil-structure interaction: A linear continuum mechanics approach (CLASSI). 1980.

[23] Lysmer J, Tabatabaie raissi J, Tajirian F, Vahdani S, Ostadan F. Sassi- A system for analysis of soil-structure interaction 1981.

[24] Çelebi E, Göktepe F, Karahan N. Non-linear finite element analysis for prediction of seismic

response of buildings considering soil-structure interaction. Nat Hazards Earth Syst Sci 2012;12:3495–505.

[25] Roesset JM. Soil structure interaction The early stages. J Appl Sci Eng 2013;16:1–8.

[26] Borja RI, Smith HA, Wu WH, Amies AP. A methodology for nonlinear soil-structure interaction effects using time-domain analysis techniques. Report No 101. 1992.

[27] Chao HY, Borja RI. Nonlinear dynamic soil-structure interaction analysis. 1998.

[28] Casciati S, Borja RI. Dynamic FE analysis of South Memnon Colossus including 3D soil–foundation–structure interaction. Comput Struct 2004;82:1719–36. doi:10.1016/j.compstruc.2004.02.026.

[29] Torabi H, Rayhani MT. Three dimensional Finite Element modeling of seismic soil–structure interaction in soft soil. Comput Geotech 2014;60:9–19. doi:10.1016/j.compgeo.2014.03.014.

[30] Brinkgreve RBJ, Engin E, Swolfs WM. Plaxis 3D. Reference manual. 2013.

[31] Schanz T, Vermeer PA, Bonnier PG. The hardening soil model: formulation and verification. Beyond 2000 Comput Geotech 1999:281–96.

[32] Benz T. Small-Strain Stiffness of Soils and its numerical consequences. University of Stuttgart, Germany, 2006.

[33] Benz T, Vermeer PA, Schwab R. A small-strain overlay model. Int J Numer Anal Methods Geomech 2009;33:25–44.

[34] Amorosi A, Boldini D, Falcone G. Numerical prediction of tunnel performance during centrifuge dynamic tests. Acta Geotech 2014;9:581–96.

[35] Amorosi A, Boldini D, di Lernia A. Modellazione numerica della risposta sismica locale: il caso di Lotung. XXV Convegno Naz. di Geotec., Edizioni AGI; 2014, p. 21–8.

[36] Régnier J, Bonilla L-F, Bard P-Y, Bertrand E, Hollender F, Kawase H, et al. International benchmark on numerical simulations for 1D, nonlinear site response (Prenolin): Verification phase based on canonical cases. Bull Seismol Soc Am 2016;106. doi:10.1785/0120150284.

[37] Amorosi A, Boldini D, di Lernia A. Seismic ground response at Lotung: Hysteretic elasto-plastic-based 3D analyses. Soil Dyn Earthq Eng 2016;85:44–61. doi:10.1016/j.soildyn.2016.03.001.

[38] Amorosi A, Boldini D, di Lernia A. Advanced numerical approaches to the seismic soil and structural response analyses. SECED 2015 “Earthquake risk Eng. Towar. a resilient world,” Cambridge, UK: 2015.

[39] Zeghal M, Elgamal A-W, Tang HT, Stepp JC. Lotung Downhole Array. II: Evaluation of Soil Nonlinear Properties. J Geotech Eng 1995;121:363–78.

[40] Li XS, Shen CK, Wang ZL. Fully Coupled Inelastic Site Response Analysis for 1986 Lotung Earthquake. J Geotech Geoenvironmental Eng 1998;124:560–73. doi:10.1061/(ASCE)1090-0241(1998)124:7(560).

[41] Borja RI, Lin C-H, Sama KM, Masada GM. Modelling non-linear ground response of non-liquefiable soils. Earthq Eng Struct Dyn 2000;29:63–83.

[42] Borja RI, Duvernay BG, Lin C-H. Ground Response in Lotung: Total Stress Analyses and Parametric Studies. J Geotech Geoenvironmental Eng 2002;128:54–63. doi:10.1061/(ASCE)1090-0241(2002)128:1(54).

[43] Lee C-P, Tsai Y-B, Wen K-L. Analysis of nonlinear site response using the LSST downhole accelerometer array data. Soil Dyn Earthq Eng 2006;26:435–60. doi:10.1016/j.soildyn.2005.10.005.

[44] Salvati LA, Pestana JM. Small-Strain Behavior of Granular Soils. II: Seismic Response Analyses and Model Evaluation. J Geotech Geoenvironmental Eng 2006;132:1082–90. doi:10.1061/(ASCE)1090-0241(2006)132:8(1082).

[45] Reyes DK, Rodriguez-Marek A, Lizcano A. A hypoplastic model for site response analysis. Soil Dyn Earthq Eng 2009;29:173–84.

[46] Amorosi A, Elia G, Boldini D, Schiavone F. Seismic ground response analysis: comparison between numerical simulations and observed array data. 5th Int. Conf. Earthq. Geotech. Eng., Santiago, Chile: 2011.

[47] Chen C-H, Lee Y-J, Jean W-Y, Katayama I, Penzien J. Correlation of predicted seismic response using hybrid modelling with EPRI/TPC lotung experimental data. Earthq Eng Struct Dyn 1990;19:993–1024. doi:10.1002/eqe.4290190706.

[48] Lin BC, Tsaur YL, Wu TH. The seismic responses of structure-viscoelastic foundation systems in time domain and power spectra. Eng Struct 1997;19:977–87. doi:10.1016/S0141-0296(97)00009-6.

[49] EPRI. Post-Earthquake analysis and data correlation for the 1/4-scale containment model of the Lotung Experiment. Report No NP-7305-SL. Palo Alto, California: 1991.

[50] Borja RI, Chao H-Y, Montáns FJ, Lin C-H. SSI Effects on Ground Motion at Lotung LSST Site. J Geotech Geoenvironmental Eng 1999;125:760–70.

[51] Roesset JM. Stiffness and Damping Coefficients of Foundations. Dyn. Response Pile Found., ASCE; 1980, p. 1–30.

[52] Gazetas G. Formulas and Charts for Impedances of Surface and Embedded Foundations. J Geotech Eng 1991;117:1363–81.

[53] Rayleigh J. The theory of sound. New York: Dover; 1945.

[54] Amorosi A, Boldini D, Elia G. Parametric study on seismic ground response by finite element modelling. Comput Geotech 2010;37:515–28.

[55] Bardet JP, Ichii K, Lin CH. EERA: A computer program for equivalent-linear earthquake site response analyses of layered soil deposits. 2000.

[56] Zienkiewicz OC, Bicanic N, Shen FQ. Earthquake Input Definition and the Trasmitting Boundary Conditions. Adv. Comput. Nonlinear Mech., Vienna: Springer Vienna; 1989, p. 109–38. doi:10.1007/978-3-7091-2828-2_3.

[57] Zienkiewicz OC, Chan AHC, Pastor M, Schrefler BA, Shiomi T. Computational geomechanics with special reference to earthquake engineering. John Wiley; 1999.

[58] Elgamal A-W, Zeghal M, Tang HT, Stepp JC. Lotung Downhole Array. I: Evaluation of Site Dynamic Properties. J Geotech Eng 1995;121:350–62.

[59] Borja RI, Chao HY, Montáns FJ, Lin CH. Nonlinear ground response at Lotung LSST site. J Geotech Geoenvironmental Eng 1999;125:187–97.

[60] De Mello VFB. The Standard Penetration Test, State Of the Art Report. IV Panam. Conf. Soil Mech. Found. Eng., San Juan, Puerto Rico: 1971.

[61] Vucetic M, Dobry R. Effect of Soil Plasticity on Cyclic Response. J Geotech Eng 1991;117:89–107.

[62] Han B, Zdravkovic L, Kontoe S. Numerical and analytical investigation of compressional wave propagation in saturated soils. Comput Geotech 2016;75:93–102. doi:10.1016/j.compgeo.2016.01.019.

[63] Bathe K-J. Finite Element Procedures. 2nd ed. Upper Saddle River, N.J.: Prentice Hall; 1996.

[64] Kontoe S, Zdravkovic l, Potts D. An assessment of time integration schemes for dynamic geotechnical problems. Comput Geotech 2008;35:253–264.

[65] Hardin BO, Drnevich VP. Shear Modulus and Damping in Soils. J Soil Mech Found Div 1972;98:667–92.

[66] Masing G. Eigenspannungen und Verfertigung bim Messing. Proc. 2nd Int. Congr. Appl. Mech., Zurich: 1926.

[67] Brinkgreve RBJ, Kappert MH, Bonnier PG. Hysteretic damping in a small-strain stiffness model. Proc. 10th Int. Symp. Numer. Model. Geomech. NUMOG 10 - Numer. Model. Geomech. NUMOG 10, 2007, p. 737–42.

[68] Jiang G-L, Tatsuoka F, Koseki J, Flora A. Inherent and stress-state-induced anisotropy in very small

strain stiffness of a sandy gravel. Géotechnique 1997;47:509–21. doi:10.1680/geot.1997.47.3.509.

[69] Jâky J. The coefficient of earth pressure at rest. J Soc Hungarian Archit Eng 1944:355–8.

[70] Stewart JP, Seed RB, Fenves GL. Empirical evaluation of inertial soil-structure interaction effects. Berkeley: 1998.

List of Figures

Fig. 17. Recorded and predicted acceleration time histories of the dynamic response of the containment structure during the LSST11 earthquake: (a, b) response at the roof (F4U), (c, d) response at the basement (F4L), (e, f) structural deformation and (g, h) rocking motion.

Fig. 18. Recorded and predicted acceleration time histories of the dynamic response of the containment structure during the LSST19 earthquake: (a, b) response at the roof (F4U), (c, d) response at the basement (F4L), (e, f) structural deformation and (g, h) rocking motion.

Fig. 19 Fourier spectra of the EW and NS components of the dynamic structural response recorded in-situ and numerically predicted at the roof (F4U) during (a, b) LSST7, (c, d) LSST11 and (e, f) LSST19 earthquakes.

Fig. 20. Amplification functions of the structural motion to the free-field ground motion for (a, b) LSST7, (c, d) LSST7 and (e, f) LSST19 seismic events.

Tables

Table 1. Properties of the modelled fixed-base SDOF structures for slenderness ratio $\underline{h} = 1$, mass ratio $\gamma_m = 0.16$ and 1.43 and different stiffness ratio ($\sigma = 5$, 10, 15).

Table 2. Properties of the modelled fixed-base SDOF structures for stiffness ratio $\sigma = 5$ and 10, mass ratio $\gamma_m = 0.16$ and different slenderness ratio ($\underline{h} = 1$, 3, 5).

Table 3. Recorded LSST earthquakes selected for FE analyses

Table 4. HSsmall model parameters used in the FE simulations of Lotung LSST case study.

Table 1.

	$\underline{h} = 1$					
	$\gamma_m = 0.16$			$\gamma_m = 1.43$		
σ	m_{str} (kg)	f_0 (Hz)	k (kN/m)	m_{str} (kg)	f_0 (Hz)	k (kN/m)
4	24795.9	10.47	107342.46	223163.3	10.47	966082.16
5	24795.9	8.38	68699.17	223163.3	8.38	618292.58
10	24795.9	4.19	17174.79	223163.3	4.19	154573.14
15	24795.9	2.79	7633.24	223163.3	2.79	68699.17

Table 2.

	$\sigma = 5$			$\sigma = 10$		
	$\gamma_m = 0.16$			$\gamma_m = 0.16$		
$\underline{h}$	m_{str} (kg)	k (kN/m)	f_0 (Hz)	m_{str} (kg)	k (kN/m)	f_0 (Hz)
1	24795.92	68699.18	8.38	24795.9	17174.79	4.19
3	74387.76	22899.73	2.79	74387.75	5724.93	1.4
5	123979.59	13739.84	1.68	123979.59	3434.96	0.84

Table 3.

Seismic event	Date	Duration (s)	Epicentral distance (km)	Magnitude (M_l)	Peak acceleration		
					EW (g)	NS (g)	V (g)
LSST7	20 May 1986	35.475	66.2	6.5	0.16	0.21	0.04
LSST11	17 July 1986	17.27	6.0	5.0	0.07	0.1	0.04
LSST19	08 December 1986	17.59	44.8	5.8	0.04	0.03	0.01

Table 4

	Silty Sand 0-17m	Sand with Gravel 17-23m	Silty clay 23-29m	Sand with Gravel 29-36m	Silty clay 36-47m
c' (kPa)	0	0	10	0	10
φ' (°)	30	35	24	37	24
OCR	-	-	5	-	5
K_0^{nc}	0.5	0.4264	0.5933	0.3982	0.5933
K_0^{oc}	-	-	1.327	-	1.327
G_0^{ref} (MPa)	90	115	65	160	65
$\gamma_{0.7}$ (%)	0.011	0.010	0.025	0.010	0.025
m	0.54	0	0.42	0	0.42
ν_{ur}	0.3	0.3	0.25	0.3	0.25
E_{ur}^{ref} (MPa)	60	119.5	65	164.5	65
E_{50}^{ref} (MPa)	20	39.83	21.67	54.81	21.67